DROPLET DYNAMICS IN CONFINED NATURAL CONVECTION FLOWS

Isadora Montenegro Bugarin

Master's Dissertation
Mechanical Sciences

Brasília, 04 de agosto de 2021

UNIVERSIDADE DE BRASÍLIA

Faculdade de Tecnologia
Departamento de Engenharia Mecânica

UNIVERSIDADE DE BRASÍLIA
FACULDADE DE TECNOLOGIA
DEPARTAMENTO DE ENGENHARIA MECÂNICA

DROPLET DYNAMICS IN CONFINED NATURAL CONVECTION FLOWS

Isadora Montenegro Bugarin

Orientador: Taygoara Felamingo de Oliveira, Dr. Univ (ENM/ UnB)

MASTER'S DISSERTATION

BRASÍLIA/DF: 23 de agosto de 2021

UNIVERSIDADE DE BRASÍLIA
FACULDADE DE TECNOLOGIA
DEPARTAMENTO DE ENGENHARIA MECÂNICA

Droplet dynamics in confined natural convection flows

Isadora Montenegro Bugarin

DISSERTAÇÃO DE MESTRADO SUBMETIDA AO DEPARTAMENTO DE ENGENHARIA MECÂNICA DA FACULDADE DE TECNOLOGIA DA UNIVERSIDADE DE BRASÍLIA COMO PARTE DOS REQUISITOS PARCIAIS PARA A OBTENÇÃO DO GRAU DE MESTRE EM MECHANICAL SCIENCES.

APROVADA POR:

Taygoara Felamingo de Oliveira, Dr. Univ (ENM/ UnB)
(Orientador)

Rafael Gabler Gontijo, Dr. Univ (ENM/ UnB)
(Examinador Interno)

Angela Ourivio Nieckele, Dr. Univ (DEM/ PUC-Rio)
(Examinadora Externa)

BRASÍLIA/DF, 23 DE AGOSTO DE 2021.

FICHA CATALOGRÁFICA

Droplet dynamics in confined natural convection flows
Dinâmica de gotas em escoamentos de convecção natural confinados
[Distrito Federal] 2021.
xv, 58 (ENM/FT/UnB, Mestre, Mechanical Sciences, 2021.
Master's Dissertation - Universidade de Brasília.
Faculdade de Tecnologia.
Departamento de Engenharia Mecânica.
Palavras-chave:
1. Escoamentos de Gota
2. Convecção Natural Confinada
3. Método Level Set
4. Fluidos Binários
5. Transferência de Calor
I. ENM/FT/UnB

REFERÊNCIA BIBLIOGRÁFICA

Bugarin, I. M.(2021). Droplet dynamics in confined natural convection flows. Master's Dissertation, Departamento de Engenharia Mecânica, Universidade de Brasília, Brasília, Distrito Federal, xv, 58

CESSÃO DE DIREITOS

NOME DO AUTOR: Isadora Montenegro Bugarin.

TÍTULO DA DISSERTAÇÃO DE MESTRADO: Dinâmica de gotas em escoamentos de convecção natural confinados.

GRAU / ANO: MESTRE / 2021

Isadora Montenegro Bugarin

Aknowledgments

First, I would like to thank my family for all the support and encouragement. You are my foundation and my inspiration. I also thank prof. Taygoara Felamingo de Oliveira for all he has taught me over the years, guiding me towards becoming a better researcher. Thank you for all the advice, the long meetings, the help, and dedication during all the time you've been my supervisor. Furthermore, I want to thank my amazing colleagues and friends who integrate the Energy and Environment Laboratory. You helped make the past two years way lighter, funnier and more special. Thanks for the countless insights and all the help during this work.

Finally, I would like to thank Coordenação de Aperfeiçoamento de Pessoal de Nível Superior (CAPES) for the support provided through scholarship grant during the completion of this work, and Serra do Facão Energia S.A. for providing financial support for the development of the project (ANEEL:P&D06899-2002/2020) - Desenvolvimento de metodologia para determinação de potencial de energia hidrocinética em usinas hidroelétricas.

Resumo

Uma extensa investigação foi realizada a respeito do movimento de uma única gota em escoamentos de convecção natural confinado. O estudo visa definir as trajetórias percorridas pela gota em diferentes condições iniciais. Nesse sentido, foram investigados os efeitos dos números de Rayleigh e Prandtl, da posição inicial das gotas e das propriedades térmicas de ambos os fluidos na dinâmica do escoamento. Além disso, a influência da gota em movimento nos processos de transferência de calor do sistema foi analisada usando o número de Nusselt. Diferenças finitas foram utilizadas para discretizar o modelo contínuo, as equações de Navier-Stokes foram resolvidas pelo método de projeção e a aproximação de Bousssineq foi assumida. O modelo bifásico foi definido pelo método Level Set de alta ordem. O escoamento pode ser caracterizado incialmente como um regime de movimento linear ou não linear, de acordo com o número de Rayleigh. Em regimes de movimento linear, a gota se move em trajetórias fechadas constantes, definindo em $Ra \sim 10^2$ uma trajetória reversível que passa periodicamente pela posição onde foi liberada e em $Ra \sim 10^3$ o mesmo caminho estacionário independente do ponto inicial . Para números de Rayleigh altos o suficiente, $Ra \geq 10^4$, as trajetórias se comportam de maneira não linear. Variando a posição inicial, a gota pode se mover em um caminho helicoidal em direção ao centro do invólucro ou se mover em um circuito fechado. O número de Prandtl afetou a amplitude do movimento para valores de Pr até aproximadamente 5. Dentro desse intervalo, à medida que Pr aumenta, o caminho descreve amplitudes mais curtas, mais perto da região central. Quando definido por valores maiores, Pr parece não afetar mais a dinâmica do escoamento. Para dois valores distintos de Pr, foram consideradas diferentes razões de condutividade térmica e capacidade calorífica. Os resultados destacam que as propriedades térmicas podem não apenas afetar a transferência de calor, mas também o comportamento da gota. Além disso, indetificou-se um aumento significativo na transferência de calor quando um gota de alta condutividade térmica se move em trajetórias fechadas próximas às paredes.

Palavras-chaves: Escoamentos de Gota; Convecção Natural Confinada; Método Level Set; Fluidos Binários; Transferência de Calor.

Abstract

An extensive investigation was carried regarding the motion of a single droplet in confined natural convection flows. The study aims to define the pathlines traveled by the drop within different initial conditions. In that sense, the effects on flow dynamics of the Rayleigh and Prandtl numbers, droplet's releasing position and both fluids' thermal properties were investigated. Furthermore, the influence of the moving droplet on the system's heat transfer processes was analyzed using the Nusselt number. Finite differences were used to discretized the continuum model, Navier-Stokes equations were solved by the projection method and the Bousssineq approximation was assumed. The two-phase model was defined using a high order Level Set method. The flow can be first characterized as either a linear or non-linear motion regime, according to the Rayleigh number. Within linear motion regimes, the droplet moves in constant closed paths, defining at $Ra \sim 10^2$ a reversible trajectory that periodically passes by the releasing position and at $Ra \sim 10^3$ the same stationary path regardless of the initial point. For high enough Rayleigh numbers, $Ra \geq 10^4$, the paths behave in a non-linear manner. By varying the releasing position, the droplet can either move in a helical path towards the enclosure's center or move in a marginal closed path. The Prandtl number was found to affect the path's amplitude for values of Pr up to approximately 5. Within that range, as Pr increases, the path describes shorter amplitudes, closer to the central region. When defined by larger values, Pr seems to no longer affect the flow's dynamics. For two distinct values of Pr, different ratios of thermal conductivity and heat capacity were considered. Results highlight that the thermal properties can not only affect heat transfer but also the droplet's behavior. Also, significant heat transfer enhancement was detected when higher thermal conductivities were considered for a droplet moving near the walls.

Key-words:Droplet flow, Confined natural convection, Level Set method, Binary fluids, Heat Transfer.

Contents

List of Figures

List of Tabels

List of Symbols

Greek Characters

α	thermal difusion coefficient
β	thermal expansion coefficient
Γ	droplet's interface
δ	Dirac delta
χ	trial pressure
ϵ	half interface width
θ	non-dimensional temperature difference
κ	thermal conductivity
λ_κ	thermal conductivity ratio
λ_C	heat capacity ratio
μ	dynamic viscosity
ν	kninematic viscosity
ρ	density
σ	surface tension
τ	virtual time
ϕ	distance function
Ω	interface's domain

Latin Characters

a	droplet radius
Ca	capillary number
C_v	heat capacity at constant volume
F_c	stress jump on the interface
g	gravity acceleration
$H(\phi)$	heaviside function
$\mathcal{H}$	droplet curvature
L	enclosure's sides length
ΔNu	Nusselt number variation
Nu	Nusselt number
Nu_{avg}	Average Nusselt number
$\mathbf{n}$	normal vector
p	pressure
Pr^{amb}	Ambient fluid Prandtl number
Pr^{drop}	Droplet fluid Prandtl number
Ra	Rayleigh number
t	time
T_H	high temperature
T_L	low temperature
$\mathbf{u}$	velocity vector
u	x-direction velocity
v	y-direction velocity
x_0	x-axis droplet releasing position
x_d	x-axis center of gravity component
x_w	shortest x-axis distance from hot wall
y_0	y-axis droplet releasing position

1 Introduction

1.1 Binary fluids, Emulsions and Droplet flows

Binary fluids and emulsions are vastly used as primary or auxiliary media in several industrial processes. Because of their multiple applicability, those fluids can be found within different industries, such as petrochemical, energy storage, pharmaceutical, and food. In that sense, the literature indicates increasing interest in the topic over the past thirty years. Though a consistent background on droplet and bubble rheology has already been established, studies regarding binary fluids within non-isotherm systems are today considerably limited.

There is a large number of technological applications of binary fluids in heat transfer processes. Zhang et al. (2012) discussed the influence of the phase change process on the natural convection of micro-encapsulated phase change material slurry (MPCMS). As an emerging technology on latent heat storage, PCM can improve thermal storage speed through natural convection. Also, the boiling of dilute emulsions has been studied as a solution for heat transfer enhancement. Though heat transfer coefficients are usually lower in miscible mixtures, when compared with the respective pure components, the boiling of immiscible mixtures can result in larger coefficients (Shadakofsky; Kulacki, 2019). Additionally, Liu et al. (2019) indicated that, under certain conditions, the thermal conductivity of oil-in-water emulsions can be significantly increased when considering smaller droplets at low concentrations.

The thermocapillary migration of liquid droplets consists of a consolidated field of binary fluids and heat transfer. Studied by several authors (Wu, 2017; Dai; Huang; Wang, 2018; Qiao et al., 2018), the phenomenon consists of driving forces arising from surface tension variations due to temperature gradients in droplets/bubbles interfaces.

Furthermore, binary fluids have been emerging as a thriving field of active fluids application. The droplets can be made of living or synthetic materials, resulting in a non-newtonian anisotropic fluid, capable of converting chemical or electromagnetic energy into mechanical work. Therefore, rheological properties might be, in some sense, controlled by external means(Aursand et al., 2016; Cates; Tjhung, 2017; Khan et al., 2018). An example of active fluids flow is presented by Cunha et al., in which the rheology of a

ferrofluid droplet in a shear flow under the influence of a magnetic field was investigated (Cunha et al., 2018).

1.2 Confined Natural Convection Flows

The Natural Convection of internal flows has been vastly studied for its complexity due to the coupling between flow and transport (Ostrach, 1988). Important in different technological fields, such as energy systems and geophysics, the topic is well-established when considering monophase media. In 1994, Assimacopoulos, Barakos, and Mitsoulis (1994) developed a numerical simulation of a natural convection flow confined in a square enclosure. Considering both laminar and turbulent regimes, the authors varied Ra and calculated the system's corresponding Nusselt number for each case. Recently, Xu, Shi, and Zhao (2017) performed a similar case using high-speed accurate Lattice-Boltzmann simulations for Rayleigh up to 10^8. Also, Pandey et al. (2019) have provided an extensive review on the topic.

The fluid media can directly affect the system's heat transfer rates. Therefore, alternative fluids with increased thermal conductivity have been investigated as potential high-performance media. In that sense, Kefayati (2016) has investigated the heat transfer and the entropy generation by the laminar natural convection of a non-Newtonian nanofluid in a porous square cavity. Using a nanofluid composed of water and high thermal conductivity copper nanoparticles, the author identified that increasing volume fractions can result in heat transfer and entropy generation intensification. Also, Gu et al. (2018) measured how the heat flux in a dense particulate media, where a natural convection flow develops, is decomposed into convection and conduction. Mehryan et al. (2019) developed a numerical simulation to investigate the natural convection of a hybrid nanofluid in the presence of an inclined magnetic field. Several other investigations were also carried within the topic (Ma et al., 2019; Meng; Zhang; Li, 2016; Mohebbi; Rashidi, 2017; Siavashi; Yousofvand; Rezanejad, 2018).

Currently, the use of binary fluids as a solution for heat transfer enhancement is still understudied. Though a thriving field, investigations considering one single or multiple droplets in non-isotherm flows are mostly concerned with thermocapillary convection systems. In that sense, the present work aims to expand the understanding of droplet motion and heat transfer rates in a two-phase confined natural convection flow.

1.3 Bibliometric Review

The present work concerns the investigation of dynamic and thermal aspects of a two-phase flow driven by natural convection in a square enclosure. Aiming to investigate the current impact of the study topic approached, a bibliometric review was conducted.

As the conceptual problem was defined, a set of key-words was selected and displayed in Table 1.

Table 1 – Key-words and synonyms used to define the data base of the bibliometric review composed by 259 documents.

Key-words and Synonyms	Number of Documents
Droplet or Bubble Droplet motion or Droplet path or Droplet migration Multiphase flow or Two-phase flow or Binary fluid or Droplet flow Heat transfer or Natural convection or Boiling or Evaporation	**259**

The analysis was divided into four periods, resulting in 259 documents produced over 50 publishing years. The documents were divided into 22 main groups containing similar terms. Table 2 indicates an expressive increase of documents over the periods. Half the articles regarding the key-words proposed were published in the last period (4), which indicates a current interest in the topic.

Table 2 – Number of publishing years and documents per period.

ID	Period	Publishing years	Documents
1	1980-1990	10	17
2	1991-2000	19	71
3	2001-2010	10	40
4	2011-2021	11	131

An overlapping map was generated to describe theme flux from one period to the other. Figure 1.1 shows the map representing the word flux over the four periods defined. The numbers inside the circles indicate the count of themes in each period, the inclined arrows mark how many new topics were aggregated and how many were disposed of, and the horizontal arrows indicate the number of topics transferred to the next period. The numbers between parenthesis represent the *Inclusion Index*, determining the total amount of themes kept between periods, divided by the number of terms in the period with fewer topics.

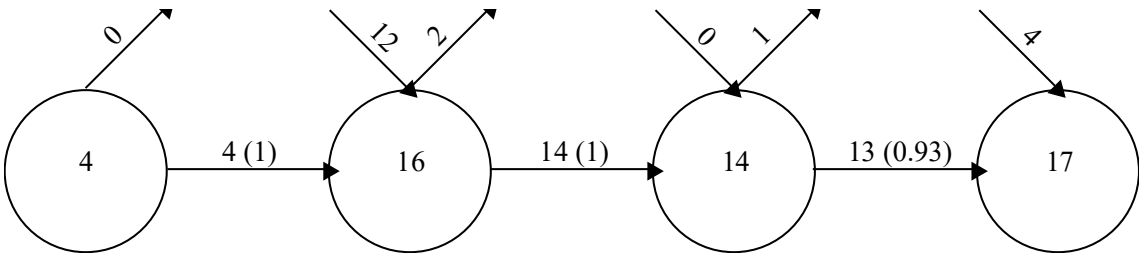

Figure 1.1 – Terms overlapping map, defined to describe the word flux over the four periods analyzed. Inclined arrows indicate the number of keywords included or eliminated at each period. The number inside the circles represents the count of relevant documents per period.

Figure 1.2 shows the main terms evolution map over the periods. The connections represent the evolution of the words into other terms. Solid lines represent the connection between clusters that share the main item, while dotted lines indicate the themes share elements, but not the main item. Line thickness is proportional to the *Inclusion Index* and the green spheres' size represents the number of documents. Conceptually, the words evolve within the same field and keeping a connection with the previous ones.

No words were detected in period 1, and consequentially no clusters were constructed. In period 2, both words appear in similar number of documents. *Convection* evolves towards the correlated topic *Heat transfer*, which in turn evolves into *Nanofluids* and *Multiphase flows*. The first evolution highlights the large number of studies on non-isotherm nanofluid flows currently displayed in the literature, as mentioned in section 1.2. The other indicates that an investigation field regarding both *Heat transfer* and *Multiphase flows* is not yet consolidated. The dotted link that connects *Convection* and *Droplets* is based on secondary related topics, which highlights the gap between both themes. *Emulsions* evolves towards *Droplets* and *Multiphase flows* through solid connections.

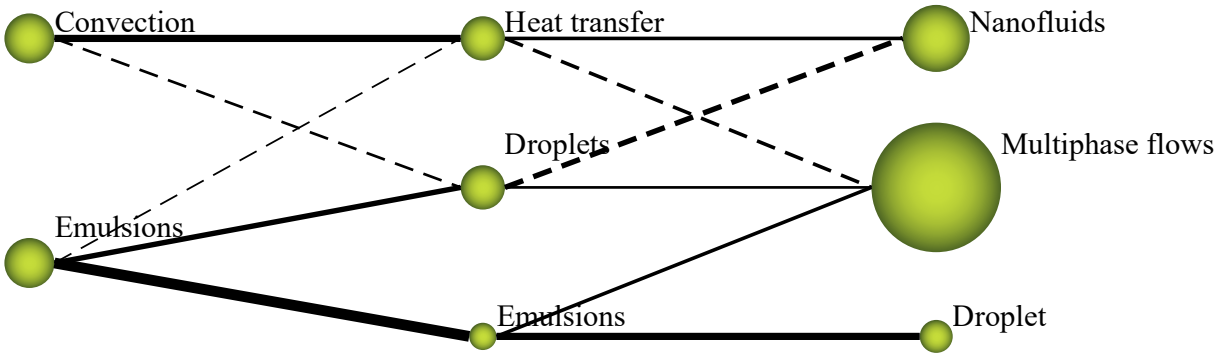

Figure 1.2 – Main terms' evolution map over the periods. Green spheres' sizes represent the document count and the line thickness is proportional to the Inclusion Index. While solid lines indicate the themes share the main item, dotted ones suggest some elements are shared.

Figure 1.3 presents the strategic diagrams of periods (a) 2, (b) 3 and (c) 4 considering the respective documents count. The diagrams characterize the clusters accordingly to their function in the network organization. The clusters are categorized according to the density and centrality, which indicates their participation in the connection's intensity measurement and the strength of the connections, respectively.

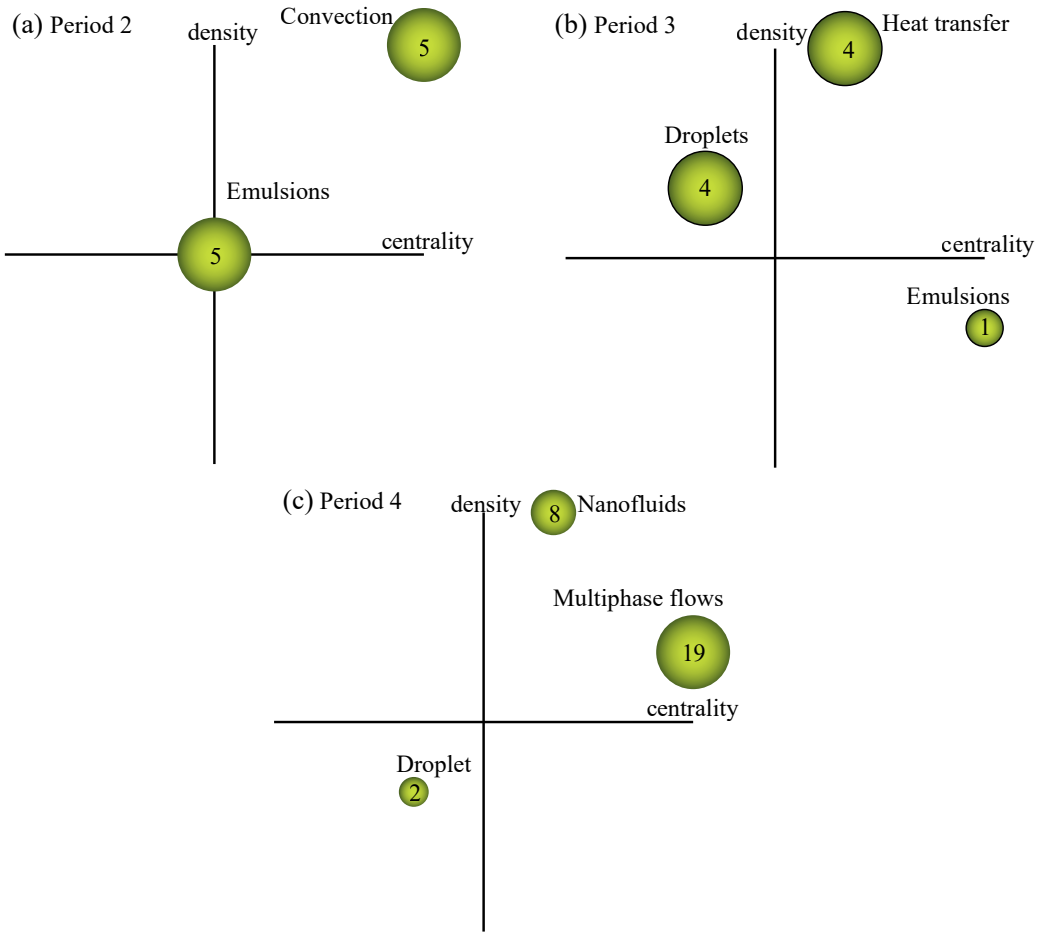

Figure 1.3 – Strategic diagrams of the three main periods (a) 2, (b) 3, and (c) 4. The measures of centrality and density are indicated and the number of documents is displayed for each theme.

Figure 1.3 (a) indicates that in the period between 1991 and 2000, the term *Convection* was highly central and developed. *Emulsions* on the other hand, appears at the intersection of the axis. In period 3, the term *Heat transfer* consists of a highly developed central term. The theme *Emulsions* now appears as a central undeveloped topic and the word *Droplet* is considered peripheral and developed. In the last period, $Multiphase flows$ is the most central term, found in the largest number of documents. $Nanofluids$ is highly developed, while *Droplet* was found to be undeveloped and peripheral.

The discussions brought up in the present work play an important role in helping fill the gaps between droplet flows and heat transfer studies. Though the topic is still rather unexplored in the literature, it consists of a current growing investigation field.

1.4 State of the Art

Classical literature is established on binary fluids under isotherm conditions. In 1973, Barthès-Biesel and Acrivos (1973) presented a theoretical methodology to predict the deformation and breakup conditions of a liquid droplet suspended in a linear shear

field. The method was developed by expanding the solution to creeping-flow equations in powers of the deformation parameter. Nayfeh's linear stability theory (1970) was applied to determine the onset of bursting. In 1994, Stone presented a complete review including theoretical, experimental, and numerical studies, that highlight the dynamics of droplet deformation and breakup in viscous fluids.

In 1972, Torza, Cox, and Mason conducted experiments on viscous droplets suspended in a shear flow. The experimental results confirmed Taylor's classical theory of small drop deformations (1932) and suggested that interfacial tensions of viscous droplets can be determined by varying drop shape oscillations in a time-dependent laminar flow.

Later on, relevant discussions on droplet deformation were brought up by Rallison in a review article published in 1984, highlighting the theoretical predictions and experimental observations available at the time. Ten years later, an updated review on the topic was present by Stone (1994). According to the author, with exception of the work of Hakimi and Schowalter (1980), which considered vorticity-dominated flows, all experimental works published before 1986 were limited to either simple shear or two-dimensional extensional flows.

Experimental investigations regarding deformation and burst of fluid droplets within linear flows were also carried by Bentley and Leal (1986). The work consists of a systematic investigation of vorticity effects in the imposed flow, where the magnitude of the strain rates surpass that of the vorticity. Comparing experimental results with previous theories, the authors indicated that over a wide range of viscous ratios, Capillary number, and flow type, considerably adequate predictions can be delivered by the theoretical knowledge consolidated so far.

Classical numerical studies on droplet shear and breakup can also be found within the literature. In 1978, Rallison and Acrivos studied deformation and the breakup conditions of a viscous droplet freely suspended in a shear flow. Numerical results showed good agreement with Taylor's small deformation (1932) and slender body (1966) theories, and with Barthès-Biesel's theory as well (1973). Later, Loewenberg and Hinch (1996) conducted a three-dimensional study of a concentrated emulsion in shear flow for low Reynolds and finite capillary number conditions. Results reveal complex rheology, as the alignment of deformed drops in the flow's direction results in an anisotropic microstructure. Pronounced shear thinning and large normal stresses were observed on the investigations carried for volume fractions up to 30%.

Due to its multiple applicability and relevant presence in the industry, a large number of studies on oil-in-water emulsions have been developed over recent years (Wang et al., 2021; Huyst et al., 2021; Liu et al., 2021; Zhou et al., 2021). Though most cases consider isotherm systems, the field has been unraveling towards temperature-dependent flows (Kempin et al., 2021; Fan et al., 2021; Khalid et al., 2020; Guo et al., 2021). Liu et al. (2019) conducted an experimental study on non-Fourier heat conduction characteristics in

oil-in-water emulsions prepared with different droplet sizes. The emulsions' effective thermal conductivity suffers non-linear variations with droplet size, fluid properties, concentration, and temperature. Results have indicated that, at low concentrations, thermal conductivity can be significantly enhanced.

Thermocapillary migration is a well-established field of binary fluids within non-isotherm systems. In 1959, Young, Goldstein, and Block wrote the pioneering work on the topic, in which they developed experiments and a linear model to predict a droplet's migration speed in a Stokes flow under the effect of a negative temperature gradient. Later, the thermocapillary migration stability of a spherical buoyant droplet moving in an unbounded quiescent fluid was analyzed by Ascoli and Lagnado (1992). More recently, Qiao et al. (2018) coupled the lattice Boltzmann and finite differences to develop a numerical scheme applied to interfacial droplets thermocapillary motion.

Furthermore, more recent work can be found on the matter of heat transfer in emulsions. Gasanov (2019) conducted an experimental work on the boiling of disperse-phase droplets in a forced flow in a circular mini channel, considering water/PMS-20 and n-pentane/glycerine emulsions with and without the use of surfactants. Results show that depending on the mass flow, the boiling of a water/PMS-20 emulsion improves the heat transfer rate at 20-35% in comparison with the monophase PMS-20. At high heating temperatures of the channel wall, the heat transfer is also improved by the boiling of n-pentane/glycerine emulsions. Also, Wenzel, Kulacki, and Garrick (2016) investigated numerically a single droplet in the boundary layer flow developed near a flat heating plate. The flow patterns as a consequence of the Reynolds, Weber, and Prandtl number were studied, indicating that the temperature field near the droplet is significantly altered by its rotation and that Magnus lift forces provoke the separation of the drop from the heated surface.

Chen et al. (2020) investigated a bubble's dynamic behavior rising near a vertical wire-mesh, analyzing the effects of the initial wall distance. Finally, Yap et al. (2019) studied the influence of particle deposition on heat transfer rates in a two-phase liquid-droplet flow in the heat exchanger. Using two Level Set functions to capture both liquid-droplet interface and liquid-deposit front, the authors observed that the deposit affects the flow and heat transfer, blocking part of the fluid passage and introducing an extra thermal resistance from the heat exchanger tube to the flow.

1.5 Objectives

The present work displays the results of a natural convection flow confined in a square enclosure, where a droplet moves driven by buoyancy. The main goal is to identify the two-dimensional drop motion patterns and their effects on heat transfer. Therefore, the paths followed by the droplet were investigated considering the influence of several

initial conditions. The study's main contribution consists of displaying innovative insights regarding the dynamics of non-isotherm binary fluids.

1.6 Objectives

The present work displays the results of a natural convection flow confined in a square enclosure, where a droplet moves driven by buoyancy. The main goal is to identify the two-dimensional drop motion patterns and their effects on heat transfer. Therefore, the paths followed by the droplet were investigated considering the influence of several initial conditions. The study's main contribution consists of displaying innovative insights regarding the dynamics of non-isotherm binary fluids.

1.6.1 Specific Objectives

- Define a numerical model to simulate a natural convection flow where a two-dimensional droplet is released;
- Implement the model from scracht using Fortran language;
- Validate the thermal and dynamics aspects separately to assure the good agreement of the simulation developed with results available at the literature;
- As the droplet's path observation is essential to the motion analysis proposed, the interface's center of mass must be defined and its position calculated, for every step;
- Simulate and display results for three distinct Rayleigh numbers, while the remaining initial conditions stay unaltered. As one of the main non-dimensional parameters of natural convection flow, Ra is expected to promote a significant influence on the flow's dynamics;
- Investigate the effects of the droplet initial position on the path, considering several different releasing positions along both the x and y-axis;
- Promote qualitative and quantitative discussions on motion patterns, flow's asymmetries, droplet deformation, and motion's turnover frequencies;
- Still varying the releasing position, the Prandtl number's effects on the path patterns must also be investigated separately. Afterward, the differences between Pr and Ra effects will be evaluated, associating the flow's behavior with the physical phenomena behind it;
- Identify the influence of the droplet's thermal conductivity and heat capacity on the system's dynamics and heat transfer;

- Finally, the effects of the moving droplet on the system's heat transfer can be observed by comparing the Nusselt number variations.

1.7 Scope

The present work has been organized as follows. Chapter 2 displays the complete mathematical formulation used to define the physical problem, as well as the non-dimensionalization terms applied to the equations. After establishing the set of equations to be numerically solved, chapter 3 brings the numerical methods applied to assure a satisfactory implementation of the mathematical model. Then, the results and discussions are presented along with chapter 4, including a grid convergence analysis, numerical validations of the code developed, and results regarding several essential aspects of the flow. To conclude, chapter 5.1 shows the author's final considerations.

2 Mathematical Formulation

2.1 Problem Statement

A two-phase laminar flow inside a square bidimensional enclosure was considered, as showed in Fig. 2.1. The ambient fluid's thermal conductivity and constant volume heat capacity are considered constant and represented by κ^{amb} and C_V^{amb}, respectively. For the droplet, those properties are given respectively by $\lambda_\kappa \kappa^{amb}$ and $\lambda_C C_V^{amb}$, where λ_κ is the ratio of thermal conductivity and λ_C is the ratio of heat capacity between the droplet and ambient fluid.

The left and right side walls are set respectively at $T_H > T_L$ and T_L. Both upper and bottom walls are thermally insulated. The display described results on a temperature gradient that, in the presence of a gravitational field, induces density variations. Those variations are responsible for the appearance of convective currents inside the enclosure.

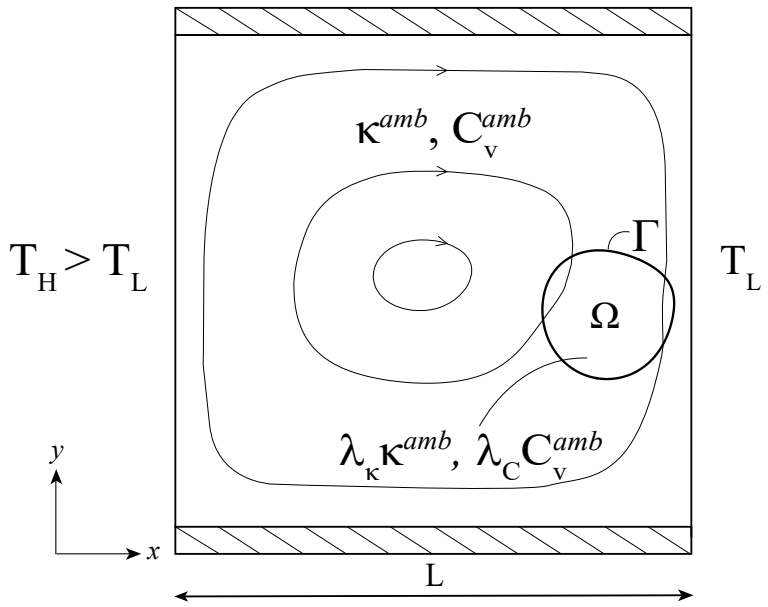

Figure 2.1 – Droplet inside an enclosure where flow driven by thermal-gravitational buoyancy develops. Left and right walls are at T_H and T_L respectively, such that $T_H > T_L$, while the top and bottom walls are insulated. The ambient fluid has thermal conductivity κ and heat capacity C_v. The droplet's fluid has thermal conductivity $\lambda_\kappa \kappa^{amb}$ and heat capacity $\lambda_C C_v^{amb}$.

2.2 Initial Conditions

All the simulations begin with a resting flow, initially set at T_L. Both disperse and ambient fluids are Newtonian and assumed to have the same density (ρ), dynamic viscosity (μ), and thermal expansion (β). The flow is incompressible and the Boussinesq approximation was assumed, which implies that the density is considered constant everywhere, with exception of the buoyancy term. The droplet radius at rest was defined as $\frac{L}{8}$, where $L = 1$ is the side of the enclosure, and the capillary number was set at 10^{-2} to prevent droplet breakup, usually associated with large deformation flow regimes.

2.3 Flow Motion Governing Equations

The equations governing the flow are the mass conservation, the linear momentum balance, and the energy conservation, given respectively by

$$\frac{\partial u^d}{\partial x^d} + \frac{\partial v^d}{\partial y^d} = 0, \tag{2.1}$$

$$\rho\frac{\partial u^d}{\partial t^d} + \rho u^d\frac{\partial u^d}{\partial x^d} + \rho v^d\frac{\partial u^d}{\partial y^d} = -\frac{\partial p^d}{\partial x^d} + \mu\left(\frac{\partial^2 u^d}{\partial {x^d}^2} + \frac{\partial^2 u^d}{\partial {y^d}^2}\right) - \sigma\mathcal{H}\delta(\phi)n_x, \tag{2.2}$$

$$\rho\frac{\partial v^d}{\partial t^d} + \rho u^d\frac{\partial v^d}{\partial x^d} + \rho v^d\frac{\partial v^d}{\partial y^d} = -\frac{\partial p^d}{\partial y^d} + \mu\left(\frac{\partial^2 v^d}{\partial {x^d}^2} + \frac{\partial^2 v^d}{\partial {y^d}^2}\right) + g\beta\rho(T_H - T_L) - \sigma\mathcal{H}\delta(\phi)n_y, \tag{2.3}$$

$$\frac{\partial T}{\partial t^d} + u^d\frac{\partial T}{\partial x^d} + v^d\frac{\partial T}{\partial y^d} = \alpha\left(\frac{\partial^2 T}{\partial {x^d}^2} + \frac{\partial^2 T}{\partial {y^d}^2}\right), \tag{2.4}$$

in which the dimensional parameters u^d and v^d, T and t^d consist of the velocities, temperature and time, respectively. Also, n_x and n_y are the outward normal vector components, $\mathcal{H} = \nabla \cdot \mathbf{n}$ is the local mean curvature, and $\delta(\phi)$ is a smoothed Dirac delta applied to the signaled distance function ϕ in the Level Set numerical context. The last terms on the RHS of equations 2.2 and 2.3 consist of the stress jump F_c on the droplet's interface, given by the Young-Laplace equation in the form of

$$F_c = \sigma\mathcal{H}\delta(\phi)\hat{\mathbf{n}}, \tag{2.5}$$

where and σ is the surface tension coefficient.

The normalization was carried out by considering L, L^2/α, and $\rho(\alpha/L)^2$ as the characteristics length, time, and pressure scales, respectively, where $\alpha = \kappa^{amb}/(\rho C_v^{amb})$ is the ambient fluid thermal diffusivity. In that sense, the non-dimensional form of the flow

governing equations is displayed next, where $\mathbf{u} = (u, v)$, t, and p are the non-dimensional velocity vector, time, and pressure, respectively. The non-dimensional temperature difference is defined by $\theta = (T - T_L)/(T_H - T_L)$.

$$\nabla \cdot \mathbf{u} = 0, \tag{2.6}$$

$$\frac{\partial u}{\partial t} + \mathbf{u} \cdot \nabla u = -\frac{\partial p}{\partial x} + Pr^{amb}\nabla^2 u - \frac{Pr^{amb}}{Ca}\,\mathcal{H}\, n_x \delta(\phi), \tag{2.7}$$

$$\frac{\partial v}{\partial t} + \mathbf{u} \cdot \nabla v = -\frac{\partial p}{\partial y} + Pr^{amb}\nabla^2 v + RaPr^{amb}\theta - \frac{Pr^{amb}}{Ca}\mathcal{H} n_y \delta(\phi), \tag{2.8}$$

$$C_v(\phi)\left(\frac{\partial \theta}{\partial t} + \mathbf{u} \cdot \nabla \theta\right) = \nabla \cdot (\kappa(\phi)\nabla\theta). \tag{2.9}$$

In Eq. 2.9, $C_v(\phi)$ and $\kappa(\phi)$ are the non-dimensional heat capacity and non-dimensional thermal conductivity, normalized by κ^{amb} and C_v^{amb}, given in the entire flow domain by

$$C_v(\phi) = \lambda_C + (1 - \lambda_C)\, H(\phi), \text{ and} \tag{2.10}$$

$$\kappa(\phi) = \lambda_\kappa + (1 - \lambda_\kappa) H(\phi), \tag{2.11}$$

where $H(\phi)$ is a smoothed Heaviside function, applied to the signaled distance. Using smoothed versions of the Dirac delta and Heaviside is in the core of the Level Set method, allowing the description of sharp variation quantities by continuum functions (Sussman et al., 1998). More details on the Level Set method will be given in section 2.4.

The dimensionless groups emerging from the normalization of the conservation equations are Prandlt (Pr^{amb}), Rayleigh (Ra), and Capillary (Ca) numbers, given, respectively, by

$$Pr^{amb} = \frac{\nu}{\alpha}, \;\; Ra = \frac{g\beta(T_h - T_l)L^3 Pr^{amb}}{\nu^2}, \text{ and } \;\; Ca = \frac{\alpha a \mu}{L^2 \sigma}. \tag{2.12}$$

In the non-dimensional parameters defined in Eq.(2.12), $\nu = \mu/\rho$ is the kinematic viscosity of the fluids and g is the gravitational acceleration. The capillary number is the ratio between the shear stress acting to deform the droplet and the surface tension restoring its circular (or spherical, when in 3D) rest shape.

2.4 Level Set Method

The Level Set method defines a signed distance function ϕ for every point in the domain to capture the drop interface Γ, given by

$$\phi(\mathbf{x}, t) = \begin{cases} -d, & \mathbf{x} \in \Omega, \\ 0, & \mathbf{x} \in \Gamma, \\ d, & \mathbf{x} \notin \Omega \end{cases} \tag{2.13}$$

where d is the distance between a point $\mathbf{x}$ and the interface, and Ω is the interior of the drop. Figure 2.2 illustrates the procedure, in which the distance between $\mathbf{x}_\Gamma$, placed on the interface, and $x \notin \Gamma$ is defined. The function $\phi(\mathbf{x})$ will be positive if $\mathbf{x}$ is placed outside the domain Ω and negative within Ω. At the interface, $\phi(\mathbf{x}_\Gamma) = 0$. The geometric properties of the droplet are also given in terms of ϕ, being the outward normal function and the average local curvature defined respectively by $\hat{\mathbf{n}} = \frac{\nabla\phi}{|\nabla\phi|}$ and $\kappa = \nabla \cdot \hat{\mathbf{n}}$.

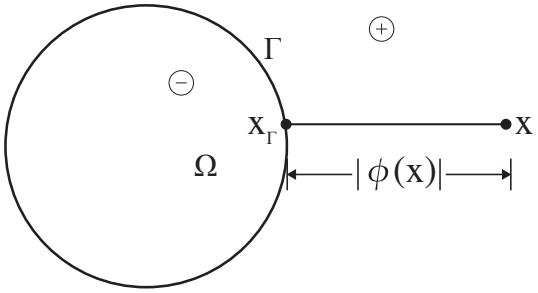

Figure 2.2 – Representation of how the Level Set function was defined. The function $\phi(\mathbf{x})$ defines the distance between the droplet's interface and the remaining points of the domain. The distance is considered positive when $\mathbf{x}$ is placed at the ambient fluid and negative when at the droplet's fluid. At the interface (Γ), $\phi(\mathbf{x}) = 0$.

As the function is not supposed to differ from $\phi = 0$ in the interface, ϕ must be a conservative function of the points in Γ. In that sense, the evolution equation is given by

$$\frac{\partial\phi}{\partial t} + \mathbf{u} \cdot \nabla\phi = 0, \tag{2.14}$$

However, as the flow develops, the distance between the remaining points in the domain ($\mathbf{x} \notin \Gamma$) and the interface should not be conserved. Those points end up deviating from their correct value as time evolution advances, causing miscalculations to the system. In order to correct that issue, one can apply a re-distancing procedure periodically. Adopting the methodology used by Sussman et. al (Sussman et al., 1998), a re-initialization equation

$$\frac{\delta\phi}{\Delta\tau} + S(\phi)[|\nabla\phi| - 1] = \lambda\delta(\phi)|\nabla\phi|, \tag{2.15}$$

was solved between three subsequent time steps, for every iteration. In Eq. 2.15, $\Delta\tau = \frac{\Delta x}{4}$ is the virtual time and $S(\phi)$ is a sign function. The RHS of the equation is a volume correction term, added to guarantee droplet area conservation. The Lagrange multiplier λ is given by

$$\lambda = \frac{\int_V \delta(\phi)(\frac{\phi^{n+1}-\phi^n}{\Delta t})dx}{\int_V \delta^2(\phi)\|\nabla\phi\|dx}, \tag{2.16}$$

where the integration should be made over the fluid domain V.

The method considers a smoothed interface of width 2ϵ. That being so, smoothed versions of the Heaviside and Dirac Delta functions are also used. In that sense, H_ϵ and δ_ϵ are given respectively by

$$H_\varepsilon(\phi) = \begin{cases} 0, & \phi < \varepsilon, \\ \frac{1}{2}\left[1 + \frac{\phi}{\varepsilon} + \frac{1}{\pi}\sin\left(\frac{\pi\phi}{\varepsilon}\right)\right], & \|\phi\| \leq \varepsilon, \\ 1, & \phi > \varepsilon \end{cases} \tag{2.17}$$

and

$$\delta_\varepsilon(\phi) = \frac{dH_\varepsilon(\phi)}{d\phi} = \begin{cases} 0, & \|\phi\| > \varepsilon, \\ \frac{1}{2\varepsilon}\left[1 + \cos\left(\frac{\pi\phi}{\varepsilon}\right)\right], & \|\phi\| \leq \varepsilon. \end{cases} \tag{2.18}$$

The half interface width was set at $\varepsilon = \frac{3}{2}\Delta x$, as it should be a small length, comparable to the grid norm.

3 Numerical Methodology

3.1 Staggered Grid

Finite differences are used to approximate all the spatial operators in an uniform rectangular cartesian staggered grid, as illustrated in Fig. 3.1. Velocity components (including the trial velocities) are stored in the grid cell faces, while the scalar quantities (p, χ, θ, ϕ) are stored in the grid cell center. The normal vector components, the curvature and the components of $\nabla\phi$ are also stored in the cell center.

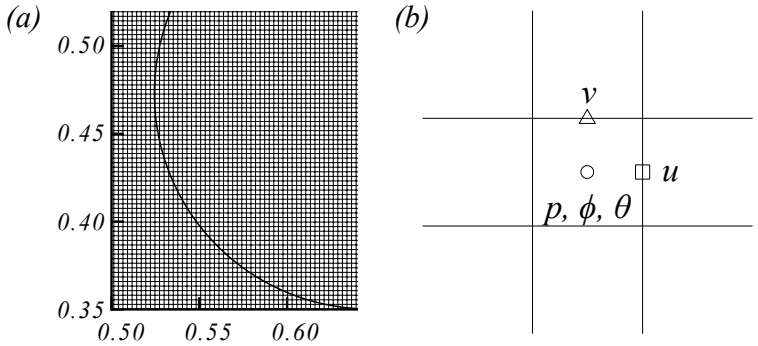

Figure 3.1 – (a) Staggered grid composed of 384^2 nodes, highlighting the actual refinement of the interface. (b) Grid cell with variables in their respective storing positions. Scalar quantities p, θ and ϕ are stored in the center of the cell, while u and v are stored respectively in the vertical and horizontal cell faces. The trial variables u^*, v^* and χ are stored in the analogous positions, and the normal vector components, the curvature and $\nabla\phi$ components are stored in the cell center as well.

3.2 Crank-Nicolson Method

While finite differences were used to approximate all spacial operators, the temporal approximation of all governing equations was done by applying the second-order Crank-Nicolson method. It consists of an implicit method in which all terms of the equation, with exception of the temporal derivative, are calculated on time $t + \frac{\Delta t}{2}$. To illustrate the

method, the discretization of Equation 2.9 is showed next, given by

$$C_v^{n+1/2}\left(\frac{\theta^{n+1}-\theta^n}{\Delta t}\right) = \nabla_h \cdot (\kappa \nabla_h \theta)^{n+1/2} - [\mathbf{u}\cdot\nabla_h\theta]^{n+1/2}, \tag{3.1}$$

where ∇_h is a discrete version of the ∇ operator. For the extrapolation of the Laplacian term, a arithmetic average value was taken, while for the convective term the second order Adam Bashforth was applied, resulting respectively in

$$\nabla_h \cdot (\kappa \nabla_h \theta)^{1/2} = \frac{\nabla_h \cdot (\kappa^{n+1}\nabla_h\theta^{n+1} + \kappa^n \nabla_h \theta^n)}{2} \tag{3.2}$$

and

$$[\mathbf{u}\cdot\nabla_h\theta]^{n+1/2} = \frac{3}{2}[\mathbf{u}\cdot\nabla_h\theta]^n - \frac{1}{2}[\mathbf{u}\cdot\nabla_h\theta]^{n-1}. \tag{3.3}$$

3.3 Projection Method

A challenge faced when solving the Navier-Stokes equations consists of separating the velocity from the pressure, as both must be calculated within the same equation. In that sense, the fractional projection method of Kim and Moin (Kim; Moin, 1985) was used to solve the mass and momentum equations, following the procedure presented in (Brown; Cortez; Minion, 2001). Equation 2.7 was discretized by

$$\frac{\mathbf{u}^* - \mathbf{u}^n}{\Delta t} = \frac{Pr^{amb}}{2}\nabla_h^2\left(\mathbf{u}^* + \mathbf{u}^n\right) + \mathcal{F}_u^{n+1/2}, \tag{3.4}$$

in which $\mathbf{u}^*$ is the trial velocity, used as an auxiliary variable. The term $\mathcal{F}_u^{n+1/2}$ stands for all the remaining terms of the equation extrapolated to $t + \Delta t/2$. The second term of the RHS of 3.4 is an approximation of the laplacian in $t + \Delta t/2$. The method also introduces a trial pressure χ, defined to assure that the Navier-Stokes formulation will stay unchanged after all equations are computed. The trial pressure equation is given by

$$\nabla_h^2 \chi^{n+1} = -\frac{\nabla_h \cdot \mathbf{u}^*}{\Delta t}, \tag{3.5}$$

where $\mathbf{u}^* = (u^*, v^*)$. The procedure consists of first calculating the trial velocities and then the trial pressure. With these results in hand, one can now apply the variables on the final velocity and pressure equations, given respectively by:

$$\mathbf{u}^{n+1} = \mathbf{u}^* - \Delta t \nabla_h \chi^{n+1} \tag{3.6}$$

and

$$p^{n+1/2} = \chi^{n+1} - \frac{Pr^{amb}}{2}\nabla_h \cdot \mathbf{u}^*. \tag{3.7}$$

3.4 Upwind Scheme

According to the convention adopted, when $u > 0$, the flow is moving from the left to right sides. In that sense, when considering the convective term $u \cdot (\partial\phi/\partial x)$ of the Level Set evolution equation 2.14, one can conclude that the approximation of the derivative of ϕ at x should be carried within the same direction. Analogously, when $u < 0$, the derivatives should be calculated from the right to left sides. That being so, the Upwind method states that the backward derivatives ϕ_x^- should be used to compute $\partial\phi/\partial x$ when $u > 0$, and the forward derivatives ϕ_x^+ should be chosen when $u < 0$ (Osher; Fedkiw, 2006).

3.5 Hamilton-Jacobi ENO

In the present work, the Hamilton-Jacobi ENO was implemented to help calculate the convective terms of equations 2.7 and 2.8. The method was applied to extend the Upwind to a second-order scheme. It consists of the extension of essentially nonoscillatory (ENO) polynomial interpolations, used to provide the smoothest polynomial interpolants, to Hamilton-Jacobi equations. The procedure allows the improvement of the first-order accurate upwind scheme, by delivering better numerical approximations to the spatial derivatives.

Considering that

$$D^-\mathbf{u} = \frac{\mathbf{u}(i) - \mathbf{u}(i-1)}{\Delta x}, \tag{3.8}$$

$$D^+\mathbf{u} = \frac{\mathbf{u}(i+1) - \mathbf{u}(i)}{\Delta x}, \tag{3.9}$$

the first divided differences can be defined as

$$D^1_{i+\frac{1}{2}}\mathbf{u} = (D^+\mathbf{u}), \tag{3.10}$$

$$D^1_{i-\frac{1}{2}}\mathbf{u} = (D^-\mathbf{u}). \tag{3.11}$$

Analogously, second divided differences are defined as

$$D^2_i\mathbf{u} = \frac{D^1_{i+\frac{1}{2}}\mathbf{u} - D^1_{i-\frac{1}{2}}\mathbf{u}}{2\Delta x}. \tag{3.12}$$

Using both first and second divided differences, one can reconstruct a second-order polynomial

$$\mathbf{u}(x) = Q_0(x) + Q_1(x) + Q_2(x), \tag{3.13}$$

in which $Q_0(x)$, $Q_1(x)$ and $Q_2(x)$ represent constant, first-order and the second-order terms, respectively. Differentiating Eq. 3.13 in $x_i = x(i)$, it results on the final derivative equation

$$\mathbf{u}_x(x_i) = Q_1'(x_i) + Q_2'(x_i). \tag{3.14}$$

With Eq. 3.14, one can calculate the smoother values of $\mathbf{u}_x^+(x_i)$ and $\mathbf{u}_x^-(x_i)$, considering that

$$Q_1'(x_i) = D^1_{k+\frac{1}{2}}\mathbf{u}, \tag{3.15}$$

$$Q_2'(x_i) = D^2_k\mathbf{u}, \tag{3.16}$$

in which $k = i$ for $(\mathbf{u}_x^+)_i$ and $k = i - 1$ for $(\mathbf{u}_x^-)_i$.

3.6 TVD Runge-Kutta

The third-order TVD Runge-Kutta was used for the temporal approximation of the Level Set evolution and re-initialization equations 2.14 and 2.15. The method develops according to five steps. The first consists of using Euler's explicit method to provide an initial trial value for ϕ^{n+1}, as shown in Eq. 3.17. The procedure is carried as follows

$$\phi^{n+1} = \phi^n - \Delta t \left[\mathbf{u} \cdot \nabla\phi\right]^n. \tag{3.17}$$

$$\phi^{n+2} = \phi^{n+1} - \Delta t[\mathbf{u} \cdot \nabla\phi]^{n+1}, \tag{3.18}$$

$$\phi^{n+\frac{3}{2}} = \phi^{n+\frac{1}{2}} - \Delta t[\mathbf{u} \cdot \nabla\phi]^{n+\frac{1}{2}}. \tag{3.19}$$

where $\phi^{n+\frac{1}{2}}$ is extrapolated to

$$\phi^{n+\frac{1}{2}} = \frac{3}{4}\phi^n + \frac{1}{4}\phi^{n+2}. \tag{3.20}$$

Finally, the distance function can be defined as

$$\phi^{n+1} = \frac{1}{3}\phi^n + \frac{2}{3}\phi^{n+\frac{3}{2}}. \tag{3.21}$$

For the solution of the re-initialization equation, the same procedure can be done, when adding the computed volume correction $\lambda\delta(\phi)|\nabla\phi|$ to ϕ^{n+1} at the end of the interpolations.

3.7 Hamilton-Jacobi WENO

When calculating the convective terms of Level Set evolution and re-initialization equations 2.14 and 2.15, the Hamilton-Jacobi WENO was used to extend the upwind first-order accurate scheme to a fifth-order spatial interpolation. It consists of a weighted combination of HJ-ENO derivatives, in which the sum of weights equals 1. According to Osher and Fedkiw (Osher; Fedkiw, 2006), the formulation is given by

$$\phi_x^1 = \frac{v_1}{3} - \frac{7v_2}{6} + \frac{11v_3}{6}, \tag{3.22}$$

$$\phi_x^2 = -\frac{v_2}{6} + \frac{5v_3}{6} + \frac{v_4}{3}, \tag{3.23}$$

$$\phi_x^3 = \frac{v_3}{3} + \frac{5v_4}{6} - \frac{v_5}{6}, \tag{3.24}$$

in which $v_1 = D^-\phi_{i-2}$, $v_2 = D^-\phi_{i-1}$, $v_3 = D^-\phi_i$, $v_4 = D^-\phi_{i+1}$ e $v_5 = D^-\phi_{i+2}$, resulting in

$$\phi_x^- = \omega_1\phi_x^1 + \omega_2\phi_x^2 + \omega_3\phi_x^3. \tag{3.25}$$

For the computation of ϕ_x^+, the analogous procedure can be done considering $v_1 = D^+\phi_{i+2}$, $v_2 = D^+\phi_{i+1}$, $v_3 = D^+\phi_i$, $v_4 = D^+\phi_{i-1}$ and $v_5 = D^+\phi_{i-2}$.

Finally, one can highlight that for obtaining optimum condition the values $\omega_1 = 0.1$, $\omega_2 = 0.6$ e $\omega_3 = 0.3$ must be set.

3.8 Boundary Conditions

The boundary conditions are applied for the trial variables and the non-dimensional temperature difference. Neumann boundary conditions were defined for χ. As the flow is surrounded by closed walls, there is no flux variation on the boundaries. In that sense,

$$\nabla\chi^{n+1} \cdot \hat{\mathbf{n}}_w = 0, \tag{3.26}$$

where $\hat{\mathbf{n}}_w$ is the outward normal vector.

Dirichet boundary conditions were applied for the trial velocities, as the non-slip condition is assumed in all four walls. Also, the implementation of the second order projection method requires corresponding adjustments on the boundary conditions. Therefore, trial velocities boundary conditions were defined as

$$\mathbf{u}^* = \mathbf{u}^{n+1} + \Delta t\nabla\chi^{n+1}. \tag{3.27}$$

To determine the conditions acting in the outward normal direction of the enclosure walls, both sides of equation 3.27 were multiplied by the outward normal vector $\hat{\mathbf{n}}_w$, as showed in Eq. 3.28.

$$\mathbf{u}^* \cdot \hat{\mathbf{n}} = \mathbf{u}^{n+1} \cdot \hat{\mathbf{n}}_w + \Delta t \nabla \chi^{n+1} \cdot \hat{\mathbf{n}}_w. \tag{3.28}$$

Eq. 3.33 shows that the last term of RHS of 3.28 equals zero, resulting in

$$\mathbf{u}^* \cdot \hat{\mathbf{n}} = \mathbf{u}^{n+1} \cdot \hat{\mathbf{n}}_w. \tag{3.29}$$

To determine the tangential boundary conditions, Eq. 3.27 is multiplied by the tangential vector $\hat{\mathbf{t}}_w$, resulting in

$$\mathbf{u}^* \cdot \hat{\mathbf{t}} = \mathbf{u}^{n+1} \cdot \hat{\mathbf{t}} + \Delta t \nabla \chi^{n+1} \cdot \hat{\mathbf{t}_w}. \tag{3.30}$$

For both vertical walls

$$\Delta t \nabla \chi^{n+1} \cdot \hat{\mathbf{t}} = \Delta t (\partial \chi / \partial y)^{n+1}, \tag{3.31}$$

and for both horizontal walls

$$\Delta t \nabla \chi^{n+1} \cdot \hat{\mathbf{t}} = \Delta t (\partial \chi / \partial x)^{n+1}. \tag{3.32}$$

As the solution is limited to the boundaries, $\mathbf{u}^{n+1} = \mathbf{u}_{wall} = 0$.

The values of θ on both vertical walls are known, therefore Dirichlet boundary conditions were applied. On the left hand side, $\theta = 1$ while on the right side $\theta = 0$. On the horizontal walls, Neumann boundary conditions were used, so that

$$\nabla \theta^{n+1} \cdot \hat{\mathbf{n}}_w = 0. \tag{3.33}$$

3.9 Linear Systems Construction

For numerical computation of the motion governing equations, linear systems were constructed according the stencil in Figure 3.1, and stored in the form

$$a(i,j) \cdot x(i-1,j) + b(i,j) \cdot x(i,j-1) + c(i,j) \cdot x(i,j) +$$

$$d(i,j) \cdot x(i+1,j) + e(i,j) \cdot x(i,j+1) = f(i,j). \tag{3.34}$$

For each equation, different values were defined for the system's components, assuring an agreement with the mathematical formulation. On equations 3.4 and 3.5, the values of a, b, c, d and e are constants calculated out of the main loop, and described as follows

$$au(i,j) = du(i,j) = av(i,j) = dv(i,j) = \frac{\Delta t Pr^{amb}}{2\Delta x^2}, \tag{3.35}$$

$$a\chi(i,j) = d\chi(i,j) = \frac{-1.0}{\Delta x^2}, \tag{3.36}$$

$$bu(i,j) = eu(i,j) = bv(i,j) = ev(i,j) = \frac{\Delta t Pr^{amb}}{2\Delta y^2}, \tag{3.37}$$

$$b\chi(i,j) = e\chi(i,j) = \frac{-1.0}{\Delta y^2}, \tag{3.38}$$

$$cu(i,j) = cv(i,j) = 1.0 + \frac{\Delta t Pr^{amb}}{\Delta x^2} + \frac{\Delta t Pr^{amb}}{\Delta y^2}, \tag{3.39}$$

$$c\chi(i,j) = \frac{2.0}{\Delta x^2} + \frac{2.0}{\Delta y^2}. \tag{3.40}$$

On the energy balance equation 3.1 however, the components vary with the distance function ϕ as it depends on the values of thermal conductivity $C_v(\phi)$ and heat conduction $\kappa(\phi)$. In that sense, a, b, c, d and e must be updated for every iteration and are give by

$$a\theta(i,j) = -\frac{\Delta t}{2C_v(i,j)^{n+1/2}} \frac{\kappa(i,j)^{n+1} + \kappa(i-1,j)^{n+1}}{2\Delta x^2}, \tag{3.41}$$

$$b\theta(i,j) = -\frac{\Delta t}{2C_v(i,j)^{n+1/2}} \frac{\kappa(i,j)^{n+1} + \kappa(i,j-1)^{n+1}}{2\Delta y^2}, \tag{3.42}$$

$$\begin{aligned} c\theta(i,j) = 1.0 + &\frac{\Delta t}{C_v(i,j)^{n+1/2}} \frac{2\kappa(i,j)^{n+1} + \kappa(i-1,j)^{n+1} + \kappa(i+1,j)^{n+1}}{4\Delta x^2} \\ &+ \frac{\Delta t}{C_v(i,j)^{n+1/2}} \frac{2\kappa(i,j)^{n+1} + \kappa(i,j-1)^{n+1} + \kappa(i,j+1)^{n+1}}{4\Delta y^2}, \end{aligned} \tag{3.43}$$

$$d\theta(i,j) = -\frac{\Delta t}{2C_v(i,j)^{n+1/2}} \frac{\kappa(i,j)^{n+1} + \kappa(i+1,j)^{n+1}}{2\Delta x^2}, \tag{3.44}$$

$$e\theta(i,j) = -\frac{\Delta t}{2C_v(i,j)^{n+1/2}} \frac{\kappa(i,j)^{n+1} + \kappa(i,j+1)^{n+1}}{2\Delta y^2}. \tag{3.45}$$

The components $f(i,j)$ for all equations must be updated in the main loop for every iteration, and are defined for trial u and v velocities, trial pressure and temperature difference respectively as

$$fu(i,j) = u(i,j)^n + \Delta t\left(-1.5(\mathbf{u}\nabla u)^n + 0.5(\mathbf{u}\nabla u)^{n-1}\right) + \frac{\Delta t Pr^{amb}}{2}\nabla^2 u^n - \frac{\Delta t Pr^{amb}}{Ca}\frac{(\mathcal{H}(i,j)+\mathcal{H}(i+1,j))}{2}\delta(\phi)\frac{\left(\frac{\partial\phi}{\partial x}(i+1,j)+\frac{\partial\phi}{\partial x}(i,j)\right)}{2}, \quad (3.46)$$

$$fv(i,j) = v(i,j)^n + \Delta t\left(-1.5(\mathbf{u}\nabla v)^n + 0.5(\mathbf{u}\nabla v)^{n-1}\right) + \frac{\Delta t Pr^{amb}}{2}\nabla^2 v^n + \frac{\Delta t Ra Pr^{amb}}{4}\left(\theta(i,j+1)^n + \theta(i,j)^n + \theta(i,j+1)^{n+1} + \theta(i,j)^{n+1}\right) - \frac{\Delta t Pr^{amb}}{Ca}\frac{(\mathcal{H}(i,j)+\mathcal{H}(i,j+1))}{2}\delta(\phi)\frac{\left(\frac{\partial\phi}{\partial y}(i,j+1)+\frac{\partial\phi}{\partial y}(i,j)\right)}{2}, \quad (3.47)$$

$$f\chi(i,j) = \frac{-1}{dt}\left(\frac{u^*(i,j)-u^*(i-1,j)}{\Delta x} + \frac{v^*(i,j)-v^*(i,j-1)}{\Delta y}\right), \quad (3.48)$$

$$f\theta(i,j) = \theta(i,j)^n + \Delta t\left(-1.5(\mathbf{u}\nabla\theta)^n + 0.5(\mathbf{u}\nabla\theta)^{n-1}\right) + \frac{\Delta t}{C_v(\phi)^{n+1/2}}\cdot\frac{[(\kappa(i+1,j)^n+\kappa(i,j))^n\cdot(\theta(i+1,j)-\theta(i,j))^n}{4dx^2} \frac{-(\kappa(i,j)+\kappa(i-1,j))^n\cdot(\theta(i,j)-\theta(i-1,j))^n]}{4\Delta x^2} + \frac{\Delta t}{C_v(\phi)^{n+1/2}}\cdot\frac{[(\kappa(i,j+1)+\kappa(i,j))^n\cdot(\theta(i,j+1)-\theta(i,j))^n}{4\Delta y^2} \frac{-(\kappa(i,j)+\kappa(i,j-1))^n\cdot(\theta(i,j)-\theta(i,j-1))^n]}{4\Delta y^2}. \quad (3.49)$$

Within the formulations presented, boundary conditions were implemented accordingly to the linear system defined in Eq. 3.34. Ghost points were considered to help determine border values. When necessary, interpolations were carried to assure that the variables were calculated in the correct storage spot.

The trial velocity u^* boundary conditions on upper and bottle enclosure walls were discretized respectively as

$$\frac{u^*(i,1)+u^*(i,0)}{2.0} = 0 \rightarrow u^*(i,1) = -u^*(i,0), \quad (3.50)$$

$$\frac{u^*(i,nju+1)+u^*(i,nju)}{2.0} = 0 \rightarrow u^*(i,nju+1) = -u^*(i,nju). \quad (3.51)$$

Substituting $u^*(i,1) = -u^*(i,0)$ and $u^*(i,nju+1) = -u^*(i,nju)$ in Eq. 3.34, cu is defined on the bottom and upper walls respectively as

$$cu(i,1) = cu(i,1) - au(i,1), \tag{3.52}$$

$$cu(i,nju) = cu(i,nju) - du(i,nju). \tag{3.53}$$

The ghost points are given respectively by

$$u^*(i,0) = \frac{\Delta t}{\Delta x}\left(4.0(\chi(i+1,1) - \chi(i,1))^n - 2.0(\chi(i+1,1) - \chi(i,1))^{n-1}\right), \tag{3.54}$$

$$u^*(i,nju+1) = \frac{\Delta t}{\Delta x}\left(4.0(\chi(i+1,njp) - \chi(i,njp))^n - 2.0(\chi(i+1,njp) - \chi(i,njp))^{n-1}\right). \tag{3.55}$$

On the left and right walls, no ghost points were defined for u^*, as the trial velocity's known value is stored right in the border of the enclosure. In that sense, the boundary conditions for each side are given respectively by

$$u(0,j) = 0.0, \tag{3.56}$$

$$u(0,nju+1) = 0.0. \tag{3.57}$$

The analogous procedure was also done for v^*, χ and θ. For θ one must notice that as the components a, b, c, d and e are not constants, the boundary conditions must be recalculated for every iteration. For $v*$, the boundary conditions e ghost points are given respectively by

$$\begin{cases} cv(1,j) = cv(i,j) - bv(1,j), \\ cv(niv,j) = cv(niv,j) - ev(niv,j), \end{cases} \tag{3.58}$$

$$v^*(i,0) = \frac{\Delta t}{\Delta y}\left(4.0(\chi(1,j+1) - \chi(1,j))^n - 2.0(\chi(1,j+1) - \chi(1,j))^{n-1}\right), \tag{3.59}$$

$$v^*(i,0) = \frac{dt}{dy}\left(4.0(\chi(nip,j+1) - \chi(nip,j))^n - 2.0(\chi(nip,j+1) - \chi(nip,j))^{n-1}\right). \tag{3.60}$$

For the trial pressure

$$\begin{cases} c\chi(1,j) = c\chi(1,j) + a\chi(1,j), \\ c\chi(nip,j) = c\chi(nip,j) + d\chi(nip,j), \end{cases} \tag{3.61}$$

$$\begin{cases} c\chi(i,1) = c\chi(i,1) + b\chi(i,1) \\ c\chi(i,njp) = c\chi(i,njp) + e\chi(i,njp) \end{cases} \tag{3.62}$$

$$\begin{cases} \chi(0,j) = 0.0, \\ \chi(nip+1,j) = 0.0. \\ \chi(i,0) = 0.0, \\ \chi(i,njp+1) = 0.0, \end{cases} \tag{3.63}$$

Finally, the respective boundary conditions and ghost points of θ are

$$\begin{cases} c\theta(1,j) = c\theta(1,j) - a\theta(1,j), \\ c\theta(nith,j) = c\theta(nith,j) - d\theta(nith,j), \end{cases} \tag{3.64}$$

$$\begin{cases} c\theta(i,1) = c\theta(i,1) + b\theta(i,1), \\ c\theta(i,njth) = c\theta(i,njth) + e\theta(i,njth), \end{cases} \tag{3.65}$$

$$\begin{cases} \chi(0,j) = 2.0T_H - \theta(1,j), \\ \chi(nip+1,j) = 2.0T_L - \theta(nip,j), \\ \chi(i,0) = 0.0, \\ \chi(i,njp+1) = 0.0. \end{cases} \tag{3.66}$$

4 Results and Discussions

4.1 Grid Convergence Analysis

The grid convergence analysis was done considering the square enclosure filled with both droplet and ambient fluid, the horizontal walls kept insulated and the vertical walls set at different temperatures. The flow properties were set at $Ra = 10^4$, $Pr^{amb} = 0.7$ and $x_0 = 0.25$. The analysis' reference parameters were the Nusselt number (Nu) and the position of the drop center of mass in the x-direction (x_d), both registered in specified time steps and calculated respectively by

$$Nu = -\int_0^1 \left(\frac{\partial \theta}{\partial x}\right)_{x=0} dy, \tag{4.1}$$

$$x_d = \frac{1}{A}\int_A \mathbf{x}.H(\phi)dA. \tag{4.2}$$

Table 3 – Grid convergence analysis for the Nusselt number (Nu). Six distinct grids were used in order to obtain the convergence rate. The ratio in the fourth column relates to the Nu rate of convergence by $2^p = \lim_{n\to\infty} \frac{Nu^h - Nu^{h/2}}{Nu^{h/2} - Nu^{h/4}}$, p is the convergence rate.

h	Nu^h	$Nu^h - Nu^{h/2}$	$\frac{Nu^h - Nu^{h/2}}{Nu^{h/2} - Nu^{h/4}}$	Conv. rate (p)
4×10^{-2}	4.5164	-0.0519	1.3316	0.4131
2×10^{-2}	4.5683	-0.0390	1.8264	0.8690
1×10^{-2}	4.6073	-0.0214	1.9187	0.9394
5×10^{-3}	4.6287	-0.0111	1.9565	0.9683
2.5×10^{-3}	4.6398	-0.0057	–	–
1.25×10^{-3}	4.6455	–	–	–

Nu and x_d were computed for progressively finer meshes, halving the grid norm each time and keeping $dt = 10^{-5}$ for all cases. The method's order of accuracy was also estimated. Tables 3 and 4 indicate $\mathcal{O}(\Delta x)$ rate of convergence. As all the spatial derivatives in the numerical scheme are $\mathcal{O}(\Delta x^2)$, and both Nu and x_d, computed respectively by Eq.4.1 and 4.2, are integral quantities, they are expected to converge at $\mathcal{O}(\Delta x)$.

Table 4 – Grid convergence analysis for the position of the droplet center of mass (x_d). The same procedure used in Nusselt analysis was applied.

h	x_d^h	$x_d^h - x_d^{h/2}$	$\frac{x_d^h - x_d^{h/2}}{x_d^{h/2} - x_d^{h/4}}$	Conv. rate (p)
4×10^{-2}	0.252258844	0.002897341	9.8072882906	3.2938
2×10^{-2}	0.2493615033	-0.0002954273	5.2238368135	2.3851
1×10^{-2}	0.2496569306	-0.0000565537	2.0264187586	1.0189
5×10^{-3}	0.2497134843	-0.0000279082	2.0514399965	1.0366
2.5×10^{-3}	0.2497413925	-0.0000136042	–	–
1.25×10^{-3}	0.2497549967	–	–	–

4.2 Numerical Verification

Willing to validate the governing equations' numerical model implementation, a mono-phase version of the problem was considered under the same boundary conditions. Comparisons of Nu for three values of Ra were done regarding numerical results reported by Barakos et al. (1994), Fusegi et al. (1991), Markatos & Pericleous (1984), and Davis (1983). Table 5 brings the results, showing a good agreement between the present work and the literature references.

Table 5 – The table shows the relation between Nusselt and Rayleigh numbers for the physical model proposed, comparing the present work results with the ones in four other papers collected on the literature.

Rayleigh	Present Work	Barakos et al. (1994)	Fusegi et al. (1991)	Markatos and Pericleous (1984)	Davis (1983)
10^3	1.112	1.114	1.105	1.108	1.118
10^4	2.236	2.245	2.302	2.201	2.243
10^5	4.503	4.510	4.646	4.430	4.519

Using Barakos et al.(1994) as reference, a qualitative comparison of the iso-temperature lines and flow streamlines was carried. The similarity of the results highlights the reliability of the method implemented.

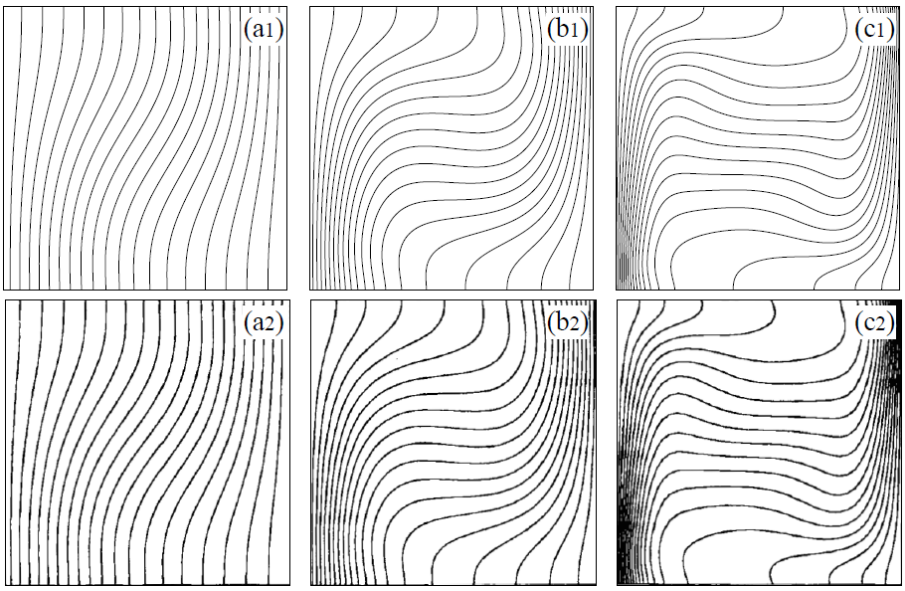

Figure 4.1 – Iso-temperature lines at different Rayleigh numbers: (a) $Ra = 10^3$, (b) $Ra = 10^4$ and (c) $Ra = 10^5$. Present work: (a1), (b1), and (c1). Reference work (Assimacopoulos; Barakos; Mitsoulis, 1994): (a2), (b2), and (c2). Reproduced with permission.

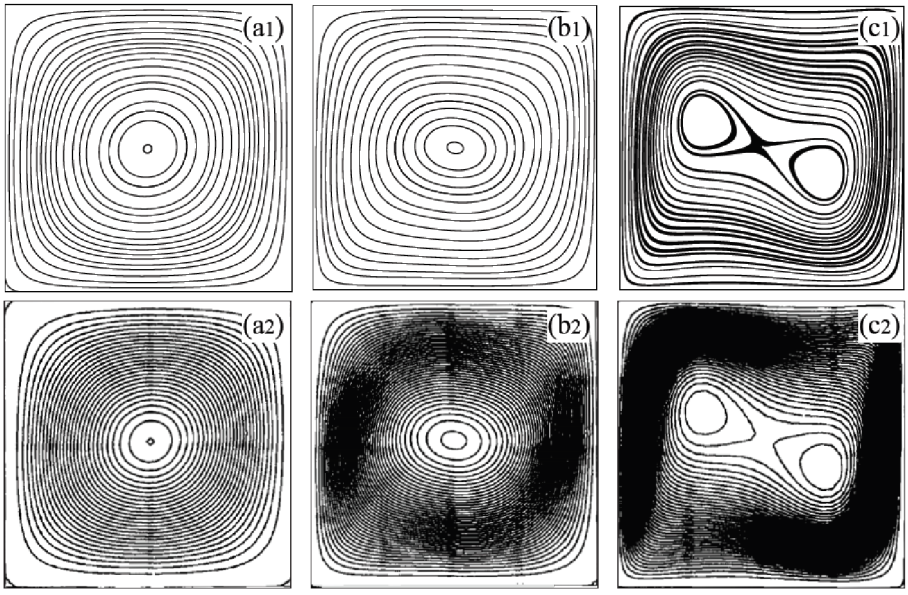

Figure 4.2 – Streamlines at different Rayleigh numbers: (a) $Ra = 10^3$, (b) $Ra = 10^4$ and (c) $Ra = 10^5$. Present work: (a1), (b1), and (c1). Reference work (Assimacopoulos; Barakos; Mitsoulis, 1994): (a2), (b2), and (c2). Reproduced with permission.

Figure 4.1 shows that at low Rayleigh numbers, vertical iso-temperature lines indicate heat is mainly transferred by conduction. As Ra enhances, convective currents begin to form near the non-adiabatic walls. Meanwhile, within the enclosure's central region the heat evolves through horizontal-like iso-temperature lines. As a result, the streamlines gradually lose their original circular shape, forming elliptical lines, as shown in Fig. 4.2. At high enough Rayleigh numbers, a second circulation region appears.

In order to guarantee that the Level Set Method was successfully implemented, a single drop in an isothermal simple shear flow, defined accordingly to Fig. 4.3, was analyzed. Considering the upper and lower walls moving with U and $-U$, respectively, periodic boundary conditions were applied on the side walls. In such a case, $Ca = \frac{\mu a \dot{\gamma}}{\sigma}$, where $\dot{\gamma} = \frac{2U}{H}$, μ is the dynamical viscosity of the droplet's fluid, H is the gap between both plates, and σ the surface tension coefficient.

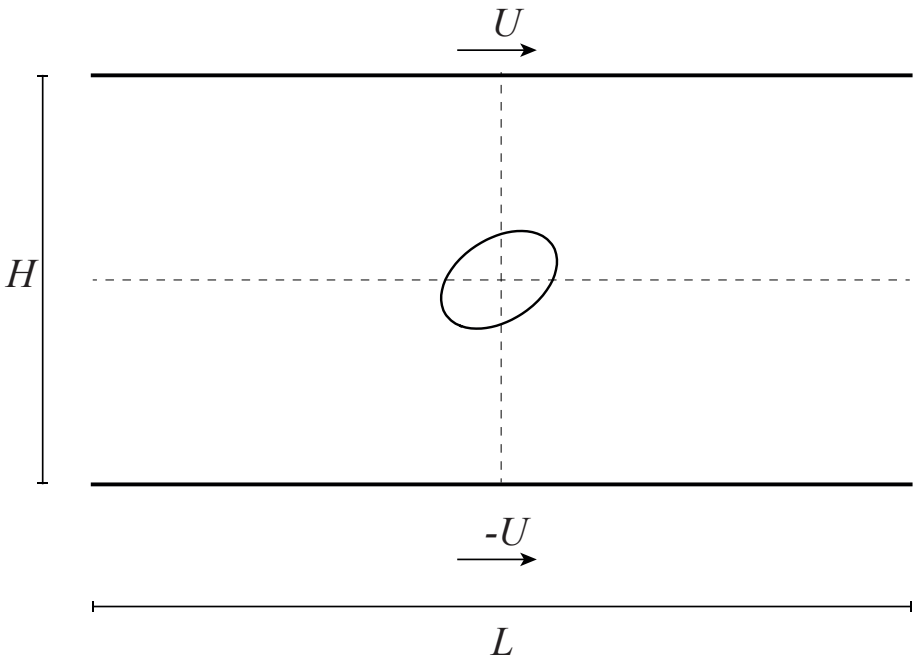

Figure 4.3 – Physical scenario considered to allow the Level Set method validation. Two equal flat plates, distanced by a lenght H, move with the same velocity U in opposite directions. A shear flow develops, occasioning droplet deformation.

Droplet deformation as a function of the capillary number was investigated and compared with previous work on the literature. The droplet deformation parameter D is defined by

$$D = \frac{B_1 - B_2}{B_1 + B_2}, \tag{4.3}$$

where B_1 and B_2 are the larger and the shorter lengths of the deformed droplet at stationary regime, respectively.

Figure 4.4 shows that larger deformations are observed when higher Capillary numbers, and consequentially lower superficial tension coefficients, are considered, facilitating shear stress deformation. Results indicate a good agreement with the reference works. Also, the present methodology has been previously validated for the simple shear case on Cunha et al. 2020. Considering that the present work is bidimensional and the reference works are all 3D, the slight divergence between the results on higher values of Ca is expected.

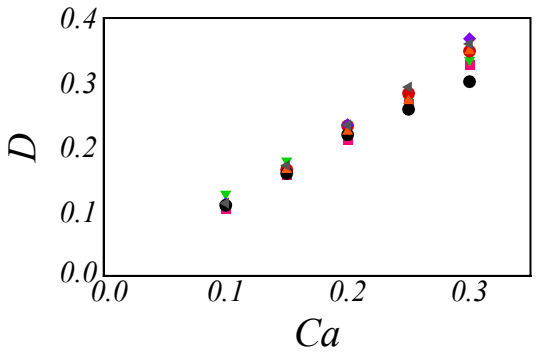

Figure 4.4 – Droplet deformation as a function of the capillary number. ●: present work; ■: Ioannou et al. (2016)(Ioannou; Liu; Zhang, 2016); ▼: Vananroye et al. (2007)(Vananroye; Puyvelde; Moldenaers, 2007); ♦: Sibillo et al. (2006)(Sibillo et al., 2006); ◀: Li et al. (2000)(Li; Renardy; Renardy, 2000); ▲: Kwak & Pozrikidis (1998)(Kwak; Pozrikidis, 1998); and ●: Kennedy et al. (1994)(Kennedy; Pozrikidis; Skalak, 1994).

4.3 Influence of the Rayleigh number on the droplet's motion

The paths followed by the droplet were investigated as a function of the Rayleigh number, which can be considered as the ratio between a time scale for diffusive thermal transport and a time scale for thermal transport by a buoyancy-driven velocity. Within the analysis, the influence of the droplet's releasing positions $\mathbf{x}_0 = (x_0, y_0)$ on the final path patterns was also studied. The droplet's area variation was controlled and its center of gravity was tracked for every iteration. All simulations start with a quiescent fluid and circular drop and proceed until the path indicates no further changes.

Unitary thermal conductivity and heat capacity ratios ($\lambda_\kappa = \lambda_C = 1$) were considered. The system's Rayleigh number was set at values up to $Ra \sim 10^4$, and the droplet was released from several distinct initial positions. Also, the Prandtl number of both fluids was kept constant and set at $Pr^{amb} = 0.70$.

Accordingly to Ra, two distinct motion regimes were identified. Within linear motion regimes, the droplet moves in closed paths passing periodically by its initial position ($Ra = 10^2$) or towards a single marginal path, regardless of the releasing point ($Ra = 10^3$). For the non-linear case at $Ra = 10^4$, the droplet can either move in helical motions towards the center or describe a single closed marginal path, depending on the releasing position.

Figures 4.5(a) and 4.5(b) show snapshots of the droplet on different positions while completing a cycle for $Ra = 10^2$ and $Ra = 10^4$, respectively. In both cases, the drop was released from $\mathbf{x}_0 = (0.25, 0.50)$. The figures also show that the motion regime directly affects droplet deformation. Under the same conditions, at $Ra = 10^4$ the droplet deformed already during the first cycle, while at $Ra = 10^2$ it conserved its circular shape, indicating that for $Ca = 10^2$, the shear stress caused by convective currents was not able to deform

the droplet. Red lines represent the path traveled by the droplet's center of mass.

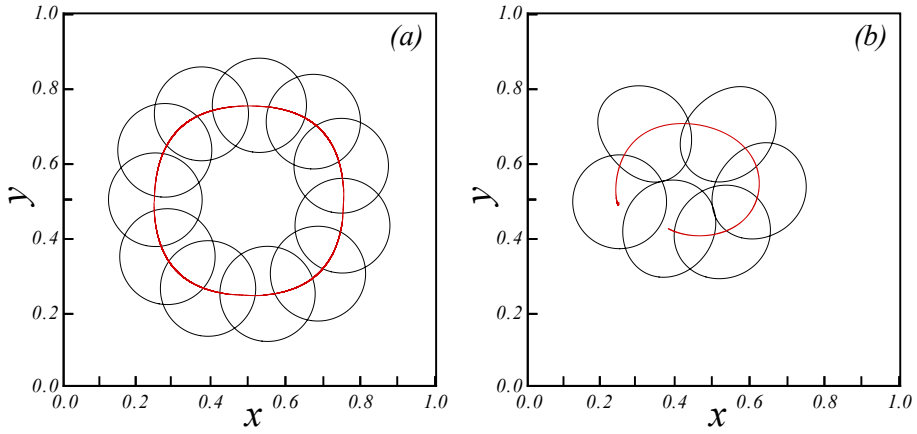

Figure 4.5 – Droplet snapshots at different positions in the first turn of its motion inside the enclosure. (a) $Ra = 1 \times 10^2$ and $x_0 = 0.25$. (b) $Ra = 1 \times 10^4$ and $x_0 = 0.25$. Droplet deformation was noticed for $Ra = 1 \times 10^4$, but not for 1×10^2. The red line is the path of the droplet's center of mass.

4.3.1 Varying the droplet's releasing position in x

For all motion regimes described, the behavior patterns were first investigated considering the nine distinct values of x_0 showed in Fig. 4.6, all evaluated at $y_0 = 0.50$.

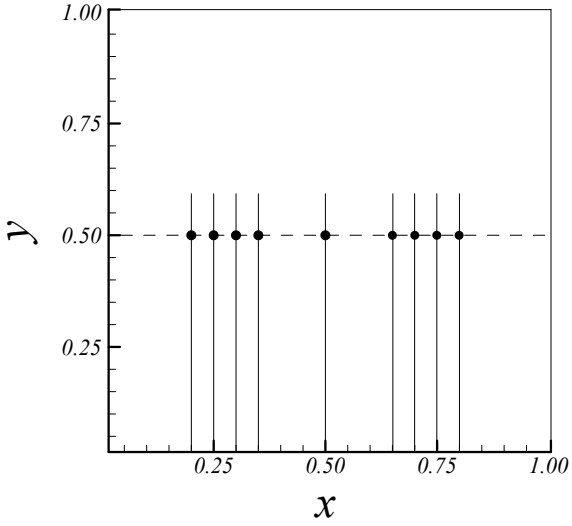

Figure 4.6 – Droplet initial positions for path patterns investigation. All resealing points are set at $y_0 = 0.5$, while x_0 varies between $0.20, 0.25, 0.30, 0.35, 0.50$, 0.65, 0.70, 0.75 and 0.80.

Figure 4.7 displays the paths observed at $Ra = 10^2$ for eight releasing positions placed on both halves of the enclosure. When released from $x_0 = 0.50$, the droplet stands still at the cavity center. For $Ra = 10^2$, the droplet moves in closed symmetrical paths,

passing periodically by its starting point. Results highlight that when released from symmetrically placed initial positions, the droplet moves within the same path. This behavior characterizes the regime as a linear flow, completely reversible in time.

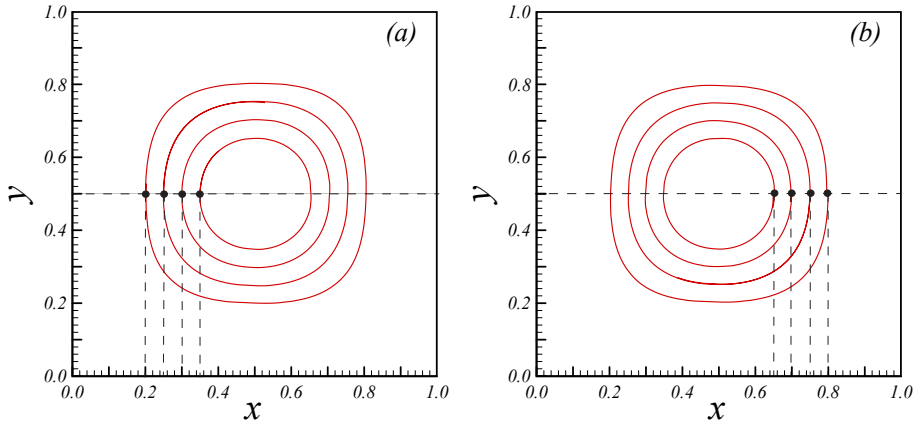

Figure 4.7 – Path patterns observed for $Ra = 10^2$. The droplet moves in closed paths, periodically passing through its releasing position. All starting points displayed in Fig.4.6 were analyzed.

For $Ra = 10^3$ a different motion pattern was observed. Regardless of the initial position, the droplet travels in periodic paths reaching one single closed path at stationary regime. Consequentially, the final distance from the droplet's center of mass and the high temperature wall (x_w) is the same for all values of x_0 evaluated. Figure 4.8 indicates that, in this case, x_0 only affects the time required to reach stationary regime. The motion begins in an asymmetric manner, eventually reaching a symmetric path. This observation elucidates that at $Ra = 10^3$, flow asymmetries start to influence the droplet's path patterns.

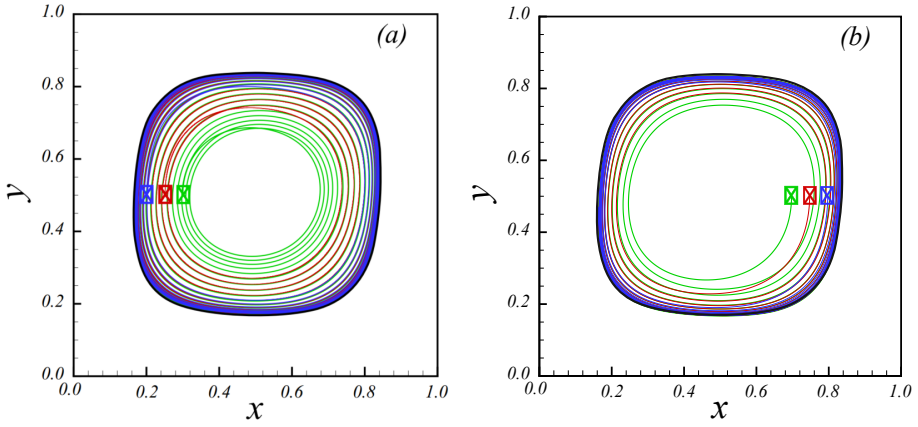

Figure 4.8 – Motion patterns observed for $Ra = 10^3$ at (a) $x_0 = 0.20$, $x_0 = 0.25$ and $x_0 = 0.30$, and (b) $x_0 = 0.70$, $x_0 = 0.75$ and $x_0 = 0.80$. Regardless of the releasing position, the droplet moves towards a single marginal path.

When analyzing the motion regime at $Ra = 10^4$, the influence of the droplet's initial position becomes more evident. In this case, depending on its starting point, the droplet can display one of two completely distinct behaviors: tracing a helical path towards

the enclosure's center or moving in periodic motions until reaching a closed marginal path. Having in mind that a droplet released from $x_0 = 0.25$ and 0.30 displays its final position at the enclosure's center, the fact that a drop placed on $x_0 = 0.50$ reaches a marginal closed path indicates a non-linear behavior.

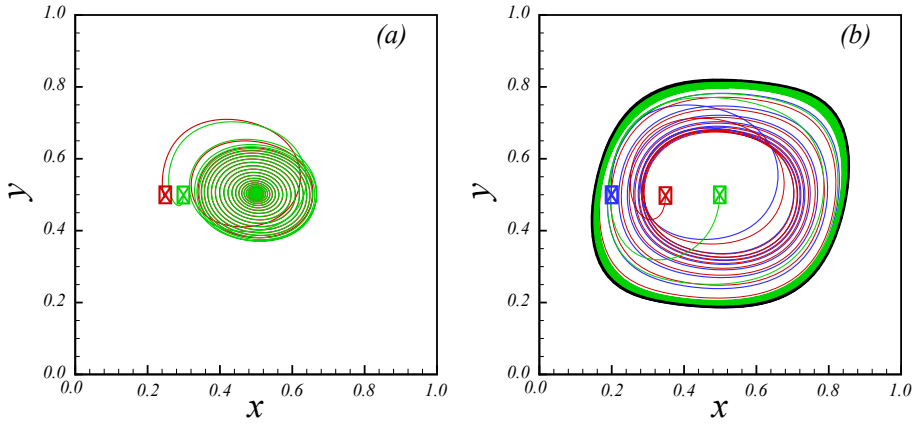

Figure 4.9 – Droplet paths observed for (a) $x_0 = 0.25$ and $x_0 = 0.30$, and (b) $x_0 = 0.20$, $x_0 = 0.35$ and 0.50. At $Ra = 10^4$, the droplet can either move in a helical motion towards the enclosure's center (a), or move in closed marginal paths (b).

Figure 4.10 shows that for $x_0 \geq 0.50$ the motion results in the same single closed path previously displayed in Fig. 4.9(b). In that sense, results indicate that none of the releasing positions placed at the cold wall half of the enclosure drives the droplet towards the central region.

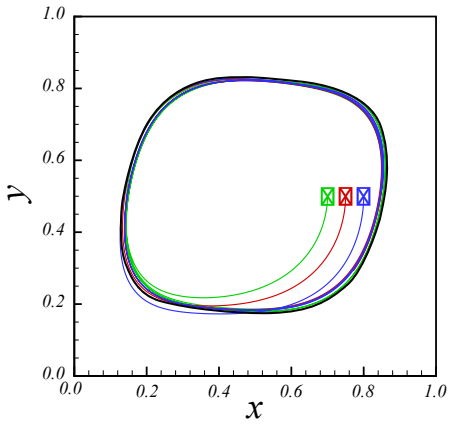

Figure 4.10 – Paths observed at $Ra = 10^4$ for $x_0 = 0.65$, $x_0 = 0.70$, $x_0 = 0.75$ and $x_0 = 0.80$. When released from the right side half of the enclosure, the droplet reaches a single closed marginal path at stationary regime for every releasing position.

Figure 4.11 displays a diagram of the smallest distance of the droplet's center of mass from the hot wall on stationary motion x_w as a function of the releasing position x_0. As specified in Fig. 4.11, $x_w = 0.50$ implies the droplet is at the enclosure's center and

$x_w = 0.15$ indicates it reached the closed marginal path near the wall region. Results for 11 equally spaced distinct values of x_0 were computed. The closed marginal path is the same for droplets released from $x_0 < 0.22$ and $x_0 > 0.32$, while in the range $0.22 \leq x_0 \leq 0.32$ the droplet always moves towards the enclosure's center.

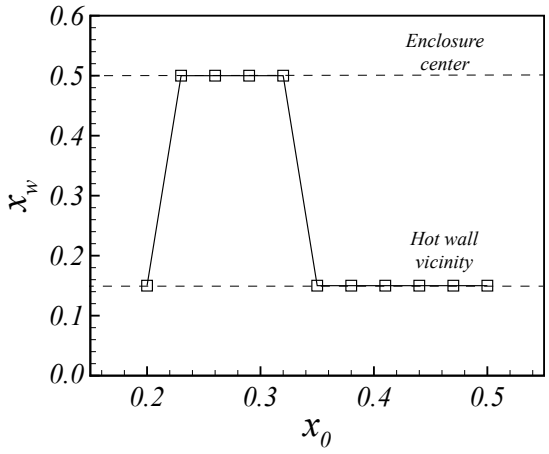

Figure 4.11 – The diagram indicates the relation between the releasing position x_0 and the path's shortest distance from the hot wall x_w. Setting $Ra = 10^4$ and $Pr^{amb} = 0.70$, the droplet moves towards the enclosure's center when $0.22 \leq x_0 \leq 0.32$.

4.3.2 Varying the droplet's releasing position in y

Previous results indicated that flow asymmetries along the x-axis have a significant influence on defining the path at high enough Rayleigh numbers. That being so, the effects of flow asymmetries along the y-axis were also investigated and the region inside the enclosure from which the droplet travels towards the center was identified. The releasing positions considered are showed in Fig. 4.12, Ra was set at 1×10^4 and two distinct values of x_0 were investigated.

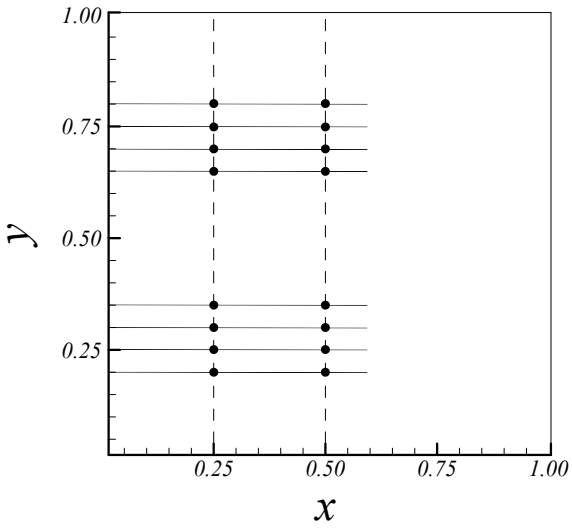

Figure 4.12 – Droplet's initial position along the y-axis. Simulations were carried considering $x_0 = 0.25$ and $x_0 = 0.50$. Analogously to the previous analysis, values of y_0 varied between $y_0 = 0.20$ and $y_0 = 0.80$.

Figure 4.13 shows that for $x_0 = 0.50$, the final path at stationary regime is the same for all eight values of y_0 analyzed. However, an evident behavior distinction can be observed when considering $y_0 < 0.50$ and $y_0 > 0.50$. This fact highlights once again the impact of flow asymmetries on the droplet's path. Soon after released from the enclosure's bottom half, the droplet is convected by the currents emerging near the high-temperature wall. On the other hand, for releasing positions defined at the upper enclosure half, the droplet moves in periodical cycles towards the marginal path.

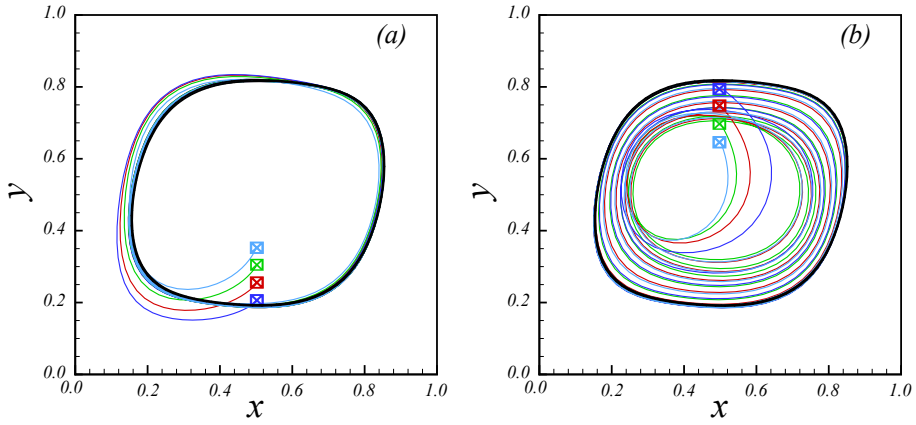

Figure 4.13 – Path patterns for varying values of y_0 evaluated for $x_0 = 0.50$. For all eight cases analyzed the droplet reaches the same marginal path.

For $x_0 = 0.25$, releasing the droplet from upper and bottom enclosure halves resulted in completely different motion behaviors. When released from the bottom half, the droplet moves near the walls rapidly reaching stationary path, as showed in Fig. 4.14 (a). For releasing positions at the upper half, the droplet moves towards the center in

helical motions. Figure 4.13 (b) shows the paths observed for $x_0 = 0.70$ and $x_0 = 0.80$, indicating that motion amplitude has considerably changed within the distinct values of y_0.

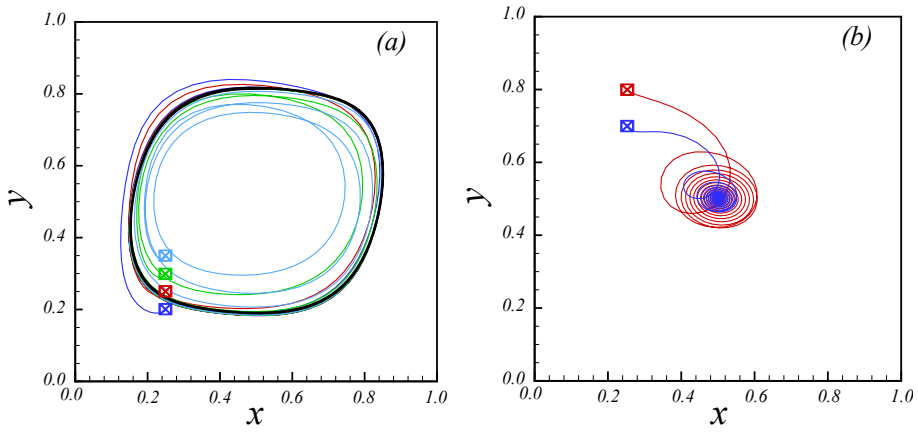

Figure 4.14 – Path patterns for the enclosure's bottom half values of y_0, all evaluated at $x_0 = 0.25$ and considering $Ra = 10^4$. The droplet reaches the same closed marginal path for each releasing position.

Within the results presented, it is possible to conclude that under the initial conditions defined, the droplet will only move towards the enclosure's when initially placed at the upper half and at the values of x_0 defined on Fig. 4.11.

4.3.3 Droplet's turnover frequency analysis

In the cases in which the path follows a marginal closed path, the horizontal coordinate of the center of mass x_d describes a sinusoidal behavior on time. Figure 4.15 shows that ω is a growing function of the Rayleigh number.

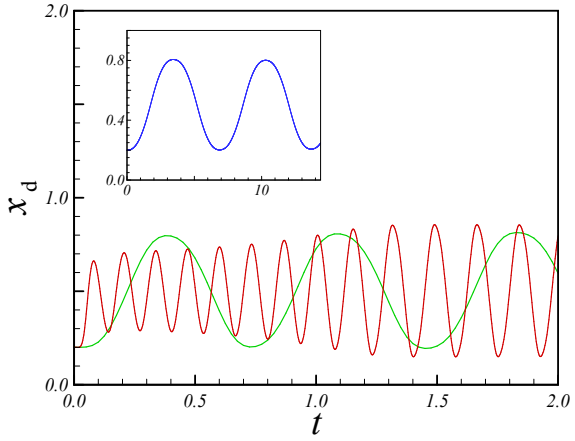

Figure 4.15 – Horizontal center of mass coordinate x_0 evaluated through time t for $Ra = 10^2$ (blue line - inset), 10^3 (green line) and 10^4 (red line). The turnover frequency seems to enhance with the Rayleigh number.

At the stationary regime, as heat conduction balances the enthalpy advection, a characteristic time of advection t_{ad} is given by

$$t_{ad} \sim \frac{\nu L}{g\alpha\beta\Delta T}. \tag{4.4}$$

Assuming that droplets are convected in the characteristic time, normalized by

$$t_c \sim \frac{L^2}{\alpha}, \tag{4.5}$$

a non-dimensional turnover frequency scales with t_c/t_{ad}, such that

$$\omega \sim Ra^{1/2}. \tag{4.6}$$

Figure 4.16 displays the non-dimensional turnover frequency as a function of $Ra^{1/2}$, analyzed for $x_0 = 0.20$. For $Ra^{1/2} \leq 100$ ($Ra \leq 10^4$) the scaling law fits very well to the simulations results. On the other hand, for $Ra^{1/2} > 100$, numerical results deviate from the scaling law drastically, indicating that on this range ω becomes a noticeably non-linear function of Ra.

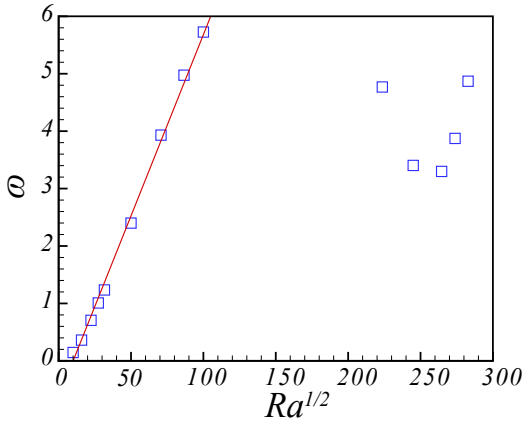

Figure 4.16 – Non-dimensional turnover frequency ω as a function of $Ra^{1/2}$.

Based on the results presented in Figure 4.16, it is possible to associate the change in the ω dependency on Ra with the formation of a second vortex in the enclosure, as shown in Fig.4.17. The second re-circulation, commonly related to high Ra regimes, is also associated with an increase on x_w, as smaller closed paths are formed near the central region.

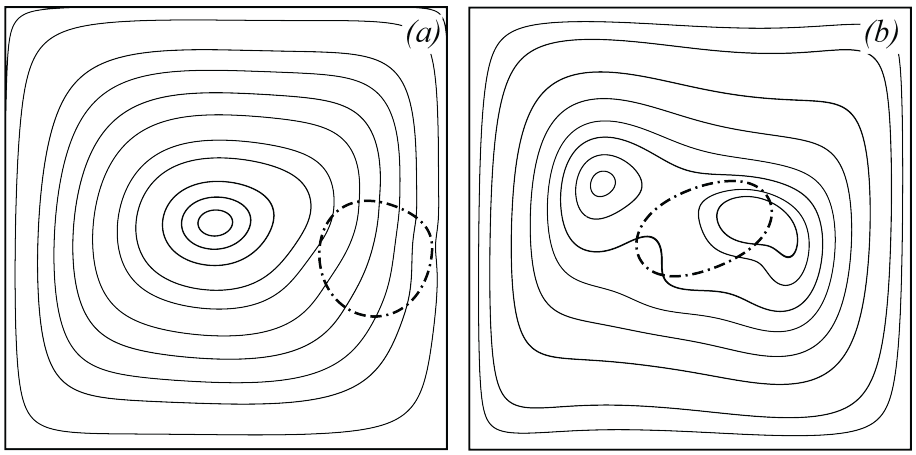

Figure 4.17 – Non-dimensional temperature difference field and streamlines for (a) $Ra = 1 \times 10^4$ and (b) $Ra = 7.5 \times 10^4$. For both cases $x_0 = 0.20$, and on (b) we observe the formation of a second vortex, as a result of the Rayleigh number enhancement.

4.4 Influence of the Prandtl number on the droplet's path

To evaluate the effects of Pr^{amb} on droplet motion, investigations considering $Pr^{amb} = 7.0$ were carried. Within the analysis, the system was kept at $\lambda_C = \lambda_\kappa = 1.0$, while different values of x_0 were investigated for $y_0 = 0.50$.

At lower Rayleigh numbers, the droplet once again behaves within linear motion regimes. Figure 4.18 (a) shows the reversible paths followed by the droplet at $Ra = 1 \times 10^2$ for both $x_0 = 0.25$ and $x_0 = 0.65$. At $Ra = 1 \times 10^3$, the motion reaches one single stationary path for both releasing positions. The final path was defined by shorter amplitudes, resulting in a larger x_w, as showed in Fig 4.18 (b).

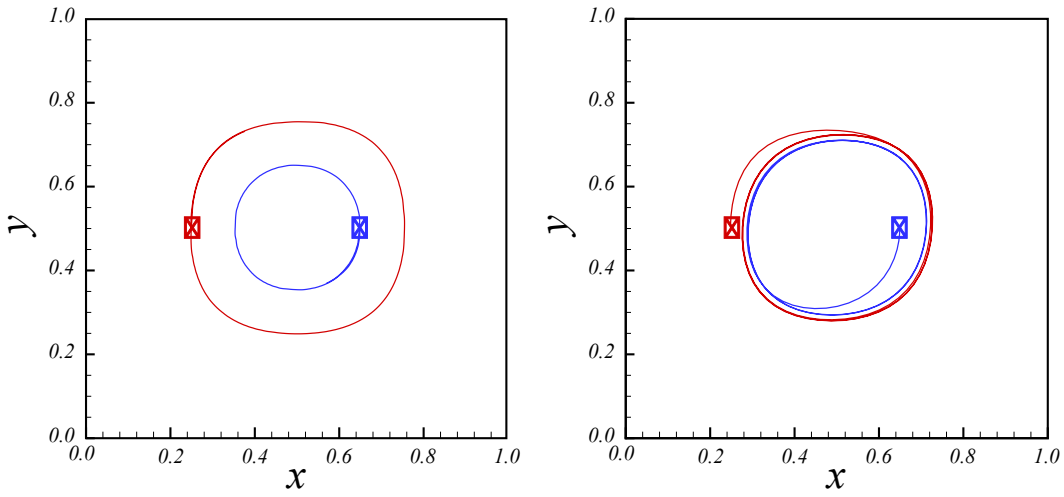

Figure 4.18 – Motion patterns registered for (a) $Ra = 10^2$ and (b) $Ra = 10^3$, both set at $Pr^{amb} = 7.0$.

For high enough Rayleigh numbers, two main aspects were noticeably affected by

the Prandtl number. Though a non-linear motion regime was detected for $Ra = 1 \times 10^4$, the range of releasing positions from which the droplet moves towards the enclosure's center has changed. Also, for the cases in which the droplet is convected by wall-region currents, the shortest distance between the stationary path and hot wall x_w has increased.

Figure 4.19 (b) indicates that the closed final path followed by the drop at stationary regime is located closer to the center, and defined by a shorter amplitude. Figure 4.19 (a) shows that for $x_0 = 0.50$ and $x_0 = 0.25$ the droplet moves towards the enclosure's center. When compared to $Pr^{amb} = 0.70$, results indicate that the flow takes longer to reach stationary regime, as the droplet moves within small amplitude variations.

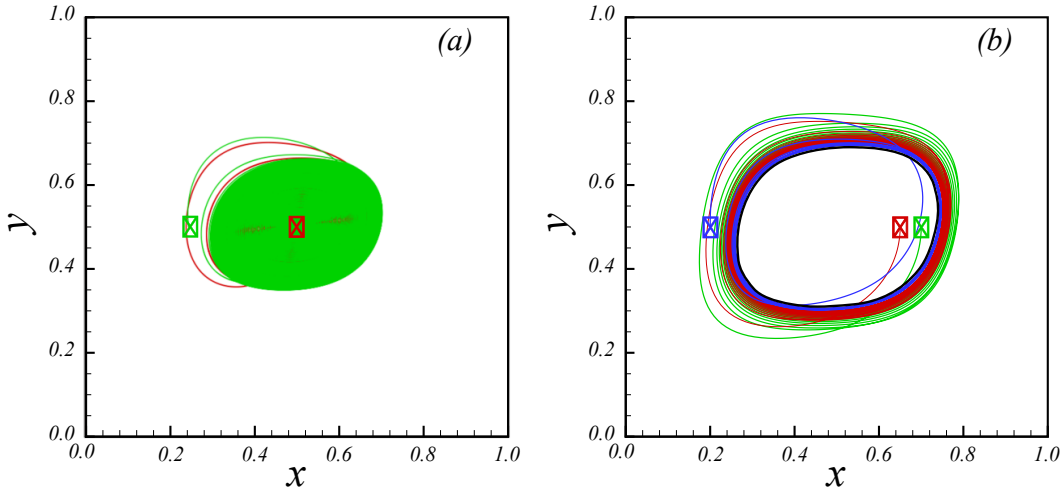

Figure 4.19 – Droplet's paths for 10^4, considering $Pr^{amb} = 7.0$. Display (a) shows the helical paths traveled by the droplet when released from $x_0 = 0.25$ and $x_0 = 0.50$. Display (b) shows the stationary path reached in cases where the droplet is convected by the wall-region currents.

To define the region inside the enclosure from which the droplet moves to the center, a diagram of x_w as a function of the releasing position x_0 was constructed. Figure 4.20 shows that for $x_0 < 0.21$ and $x_0 > 0.58$, the droplet moves in a closed limit cycle, while for $0.22 \leq x_0 \leq 0.57$ it moves towards the center. Comparing Fig. 4.11 and Fig. 4.20, one can see that the range of releasing positions from which the droplet moves towards the enclosure's center has enhanced for $Pr^{amb} = 7.0$, being 3.5 times larger than for $Pr^{amb} = 0.70$.

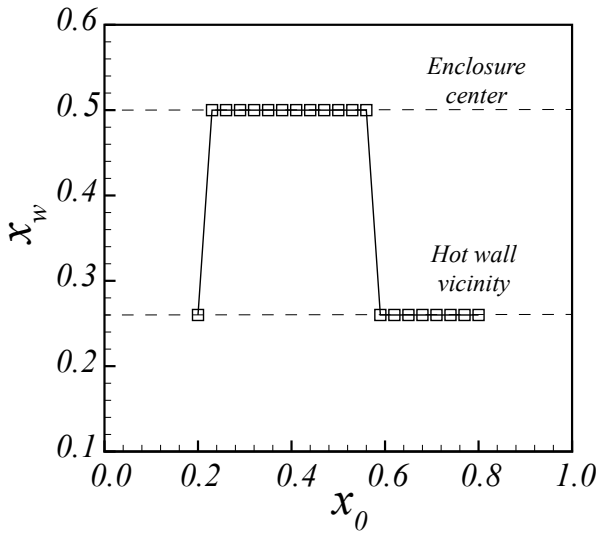

Figure 4.20 – The diagram correlates the releasing position with the final path, indicating whether the droplet moves towards the enclosure's margin ($x_0 = 0.26$) or center ($x_0 = 0.50$), when $Pr^{amb} = 7.0$.

The relation between Pr^{amb} and x_w was also studied. Considering $Ra = 1 \times 10^4$ and $x_0 = 0.20$, the values of x_w were investigated within a range of $1 \leq Pr^{amb} \leq 20$. Figure 4.21 shows that x_w varies with Pr^{amb} for values up to approximately $Pr^{amb} = 5.0$. Within values up to $Pr^{amb} = 3$, the variation is noticeably linear. For $5 \leq Pr \leq 20$, the closed marginal path stays unaltered, as x_w remains the same regardless of the Prandtl number. Results indicate that droplet motion is only affected by lower values of Pr^{amb}. For high enough Prandtl numbers, $x_w = 0.26$.

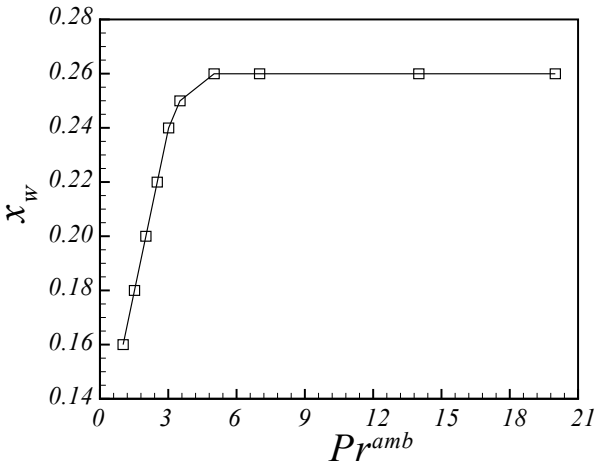

Figure 4.21 – Shortest distance between the stationary path x_0 and the hot wall as a function of the Prandtl number Pr^{amb}. For values of Pr up to 3.0, x_w varies linearly. For high enough Prandtl numbers x_w remains constant at 0.26, regardless of Pr^{amb}.

4.5 Droplet motion and temperature field

In the present model, the temperature field evolves from the high-temperature wall, as showed in Fig. 4.22. Therefore, a circulation region is formed at the enclosure's left side, moving towards the central region as the flow develops. Results have stated that depending on its releasing position, the droplet is either convected by the currents near the non-adiabatic walls or captured by that main circulation region. In that sense, for both cases the temperature difference field, velocity streamlines and interface deformation were investigated at the flow's initial moments and at stationary regime. The following analysis considers $Pr^{amb} = 0.70$ and unitary thermal properties.

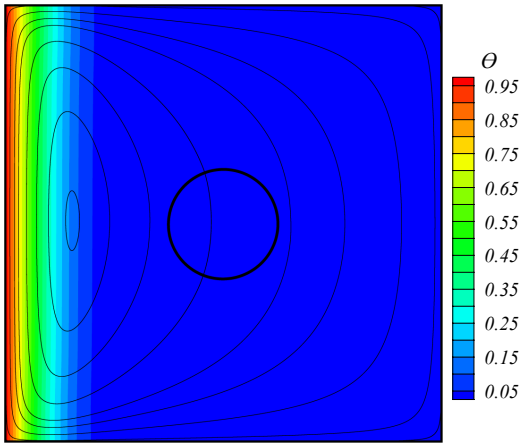

Figure 4.22 – Flow at the initial moments of the motion, considering a droplet released from $x_0 = 0.50$. The temperature difference field evolves from the high-temperature wall towards the low-temperature one. A circulation region is formed near the hot wall as the flow starts developing.

Considering the linear motion regimes, Figs. 4.23(a) and 4.23 (b) highlight the flow's divergences for $Ra = 1 \times 10^2$ and $Ra = 1 \times 10^3$, respectively. At $Ra = 1 \times 10^2$, the vertical temperature lines indicate that heat is mainly transferred by conduction. In that sense, no convective currents were developed near the non-adiabatic walls. The droplet describes a reversible motion during which the interface suffers no noticeable deformation, and the streamlines remain symmetrical, as the droplet performs no significant alterations on neither the velocity or temperature fields. For $Ra = 1 \times 10^3$, on the other hand, the flow starts to transition between conductive and convective regimes. Therefore, it is possible to observe the formation of wall-region currents that affect droplet motion and deformation, resulting in a symmetry rupture.

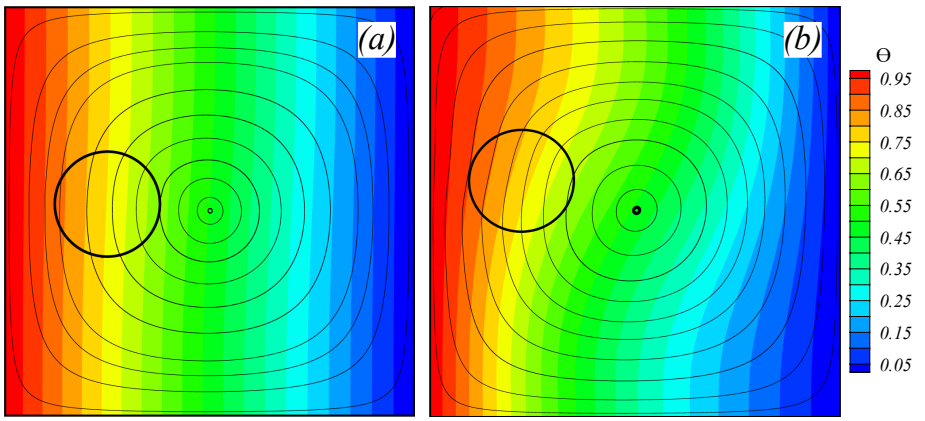

Figure 4.23 – Snapshots of the flow at stationary regime are displayed for (a) $Ra = 10^2$ and (b) $Ra = 10^3$. The interaction between the interface and both the velocity streamlines and temperature difference field are presented, highlighting the asymmetries caused by Rayleigh enhancement.

Figures 4.24 and 4.25 respectively display snapshots of the droplet's first cycle for $x_0 = 0.20$ and $x_0 = 0.50$, considering $Ra = 1 \times 10^4$. When released from $x_0 = 0.20$, the droplet is initially placed between the core circulation and the hot wall currents, suffering opposite efforts from both regions that result in a considerable interface deformation. As the droplet moves driven by the convective currents, the interface is distanced from the core circulation, moving towards the margin and considerably affecting the temperature field evolution.

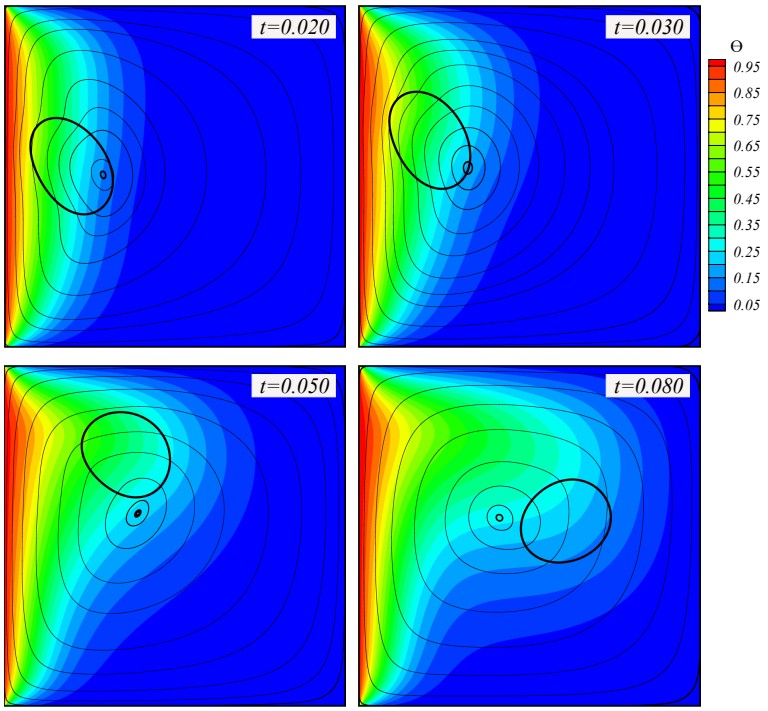

Figure 4.24 – Droplet moving in the developing flow for $Ra = 10^4$ and $Pr^{amb} = 0.70$, considering $x_0 = 0.20$. As the interface is convected by wall-region currents, the streamlines and θ field are more affected by the motion.

Releasing the droplet at the center of the enclosure, where $x_0 = 0.50$, results in

the same stationary path, but in a different trajectory, as depicted previously in Fig. 4.9. Figure 4.25 shows that, in this case, the droplet does not interact directly with the core circulation, but moves around it instead. Also, the interface does not seem to suffer any relevant attractive efforts by the core circulation. As the drop approaches the hot-wall region, it is shortly convected by the currents, causing larger interface deformations and the subtle displacement of the core circulation. Once again, the temperature field is influenced by the droplet's presence.

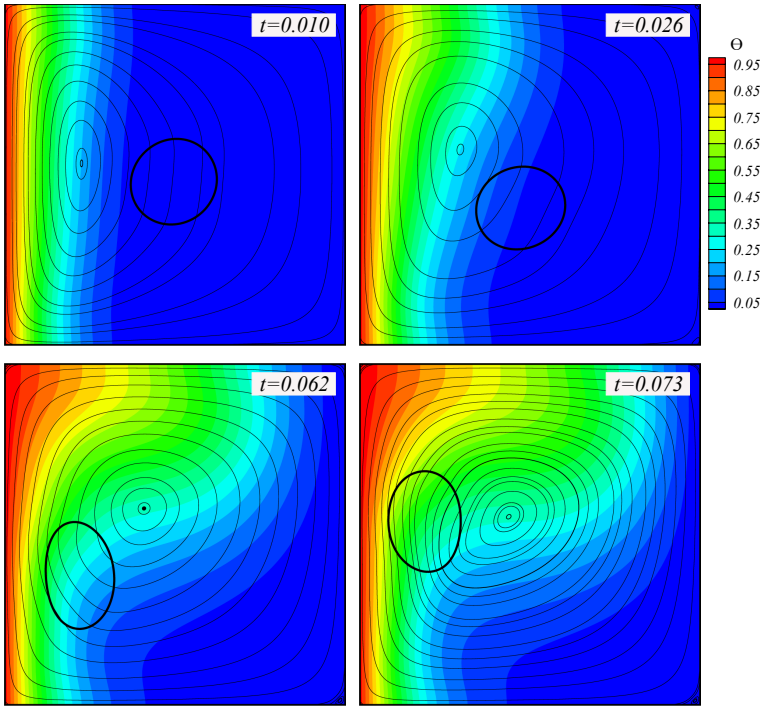

Figure 4.25 – When released from the enclosure's center, the interface moves around the core circulation, displacing it towards the opposite direction. The same happens when $x_0 > 0.50$, which highlights the fact that when released from the side where no circulation is initially developed, the droplet does not interact with the core circulation. The snapshots represent a flow set at $Ra = 10^4$ and $Pr^{amb} = 0.70$.

At stationary regime, the droplet moves near the walls, deforming continuously in a non-linear manner. Figure 4.26 shows that the core circulation region is clearly displaced by the passage of the interface. As it moves closer to the boundaries, the droplet can reach higher or lower temperatures. In contrast, in the cases which it remains at the enclosure's center, the droplet's θ stays constant at approximately the average temperature, as shows Fig. 4.28.

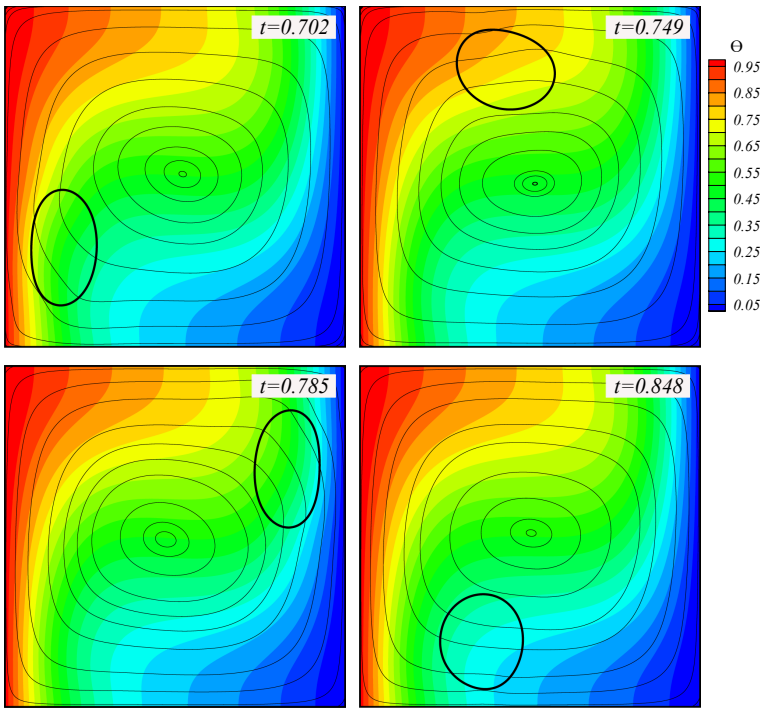

Figure 4.26 – At stationary regime, when released from $x_0 = 0.50$, the droplet moves within closed cycles near the walls suffering irregular deformations along the path. The passage of the interface results on the displacement of the core circulation, intensifying flow asymmetries.

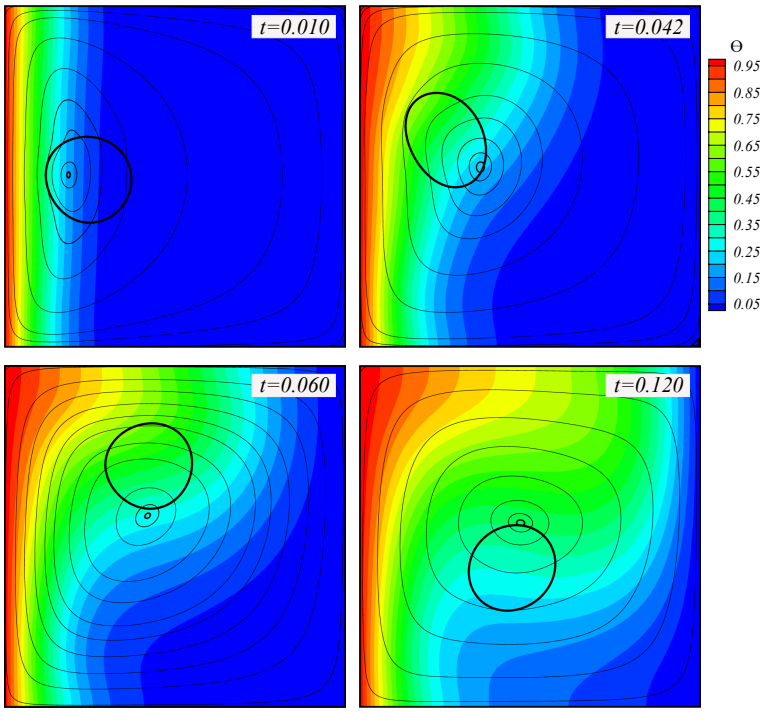

Figure 4.27 – The droplet moves towards the enclosure's center when released at the region where the core circulation develops, but not close enough to the hot wall where the convective currents are being formed. That being so, right at the beginning of the simulation, the motion is defined by the core circulation migration. The case presented consists of a droplet released at 0.25, in a flow set at $Ra = 10^4$ and $Pr^{amb} = 0.70$.

In all cases which the droplet moves towards the enclosure's center, the core circulation displays an essential influence on the flow's dynamics. It has become clear that, under constant conditions, the initial position from which the droplet is released defines whether it will be captured by the boundary region's currents or the core circulation. This phenomenon is directly related to the interface's proximity to the developing circulation region at the motion initial moments. Figure 4.27 shows the flow's evolution when releasing a droplet at $x_0 = 0.25$. The interface is captured by the circulation core already in the first cycle of its motion, displaying no relevant interaction with the convective currents emerging near the hot wall.

As the droplet remains in the central region during the entire motion, the temperature field is barely influenced by its presence. Also, the droplet reaches lower temperatures, settling at a constant temperature at stationary regime. Figure 4.28 shows that even though the interface affects the streamlines, causing the inclination of the core circulation towards the secondary diagonal, the flow recovers its symmetry. As the droplet stays still and at constant temperature, suffering no further deformations nor provoking significant changes to the flow, it is possible to conclude that the flow reaches steady state.

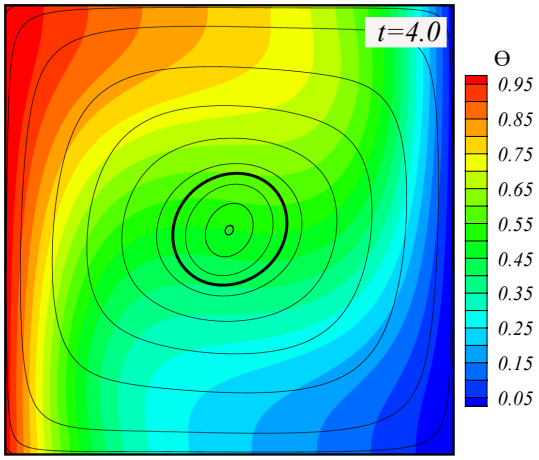

Figure 4.28 – When the droplet settles at the center, the flows recovers its symmetry. As the droplet stops deforming, the core circulation is shaped according to the interface's constant shape.

In conclusion, within the non-linear motion regime, droplet's initial position will define if and how the flow's circulation core interacts with the interface at the beginning of the motion. On its turn, the binary relation between the drop and main circulation caused by flow asymmetries are responsible for the non-linear behavior observed at high enough Rayleigh numbers.

4.6 Thermal properties influence on the droplet's path

The investigation aims to highlight how a droplet of enhanced thermal properties fluid can affect the system's dynamics. In that sense, the effects of three distinct values of

λ_κ and λ_C (1, 10 and 50) were considered within two distinct releasing positions for each value of Pr^{amb} analyzed. Both thermal properties were studied separately.

By defining the thermal conductivity and heat capacity ratios, it is also possible to determine the droplet's Prandtl number. Equation 4.7 indicates there is a linear relation between λ_C/λ_κ and Pr^{drop}, in which increasing values of λ_C define $Pr^{drop} > Pr^{amb}$, while increasing values of λ_κ result in $Pr^{drop} < Pr^{amb}$. The equation also suggests that by considering $\lambda_C = \lambda_\kappa = 1.0$, both fluids are assumed to have the same Prandtl number. In that sense, the following results highlight the effects of Pr^{drop} on droplet motion as well.

$$Pr^{drop} = \frac{\lambda_C}{\lambda_\kappa} Pr^{amb}. \tag{4.7}$$

Results displayed on Figure 4.29 show the analysis for $Pr^{amb} = 0.70$. On Figures 4.29(a) and (b), $\lambda_C = 1$ (red line), $\lambda_C = 10$ (green line) and $\lambda_C = 50$ (blue line) are compared for $x_0 = 0.25$ and $x_0 = 0.35$, respectively. For higher values of the droplet's fluid heat capacity, on both cases, rotating short helical paths are described, leading the drop towards the enclosure's center. Although the motions end at the same stationary position on the center, the paths described for $\lambda_C = 10$ and $\lambda_C = 50$ are noticeably different from the one defined for $\lambda_C = 1$, under the same circumstances (See Figure 4.29(a)).

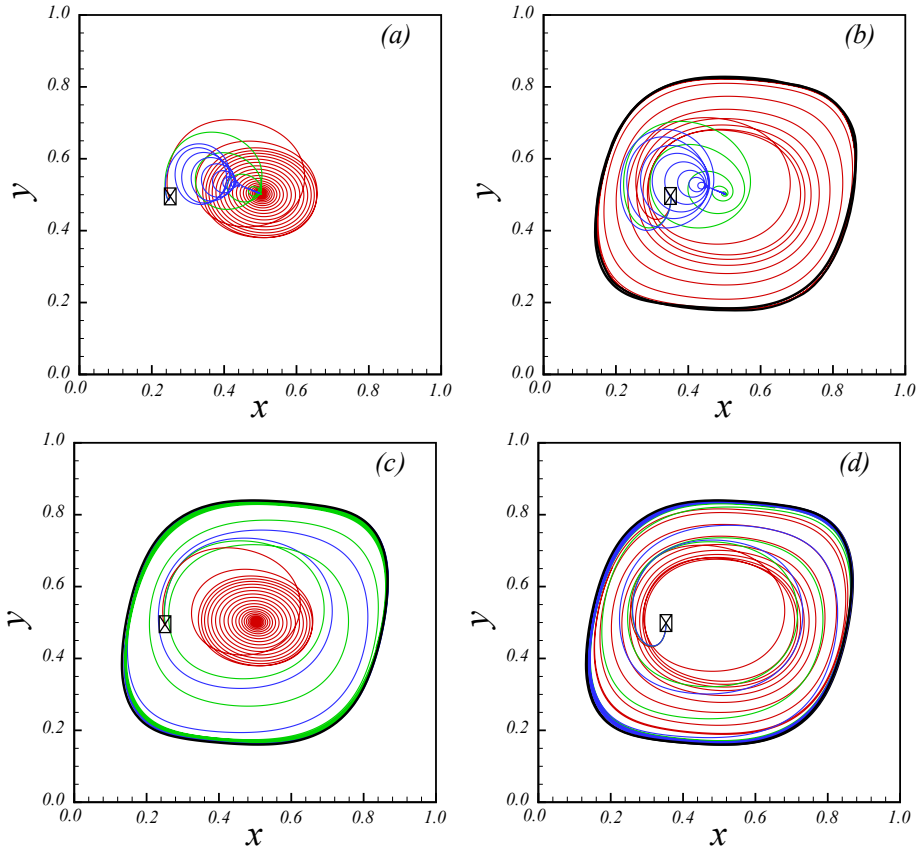

Figure 4.29 – Motion patterns defined by different heat capacity, (a) and (b), and thermal conductivity, (c) and (d), ratios varying between 1 (red lines), 10 (green lines) and 50 (blue lines). Set at $Ra = 10^4$ and $Pr^{amb} = 0.70$, (a) and (c) represent $x_0 = 0.25$, and (c) and (d) represent $x_0 = 0.35$.

For increasing values of λ_κ, on the other hand, the drop reaches a single closed marginal path for both values of x_0. Figure 4.29 shows the results for $\lambda_\kappa = 1$ (red line), $\lambda_\kappa = 10$ (green line) and $\lambda_\kappa = 50$ (blue line). The stationary path is exactly the same observed for $\lambda_\kappa = 1$.

In analogy, investigations were also carried for $Pr^{amb} = 7.0$ considering the same three ratios of heat capacity and thermal conductivity. The properties were investigated for $x_0 = 0.20$ and $x_0 = 0.35$, as these releasing positions delivered different paths for $\lambda_C = \lambda_\kappa = 1.0$.

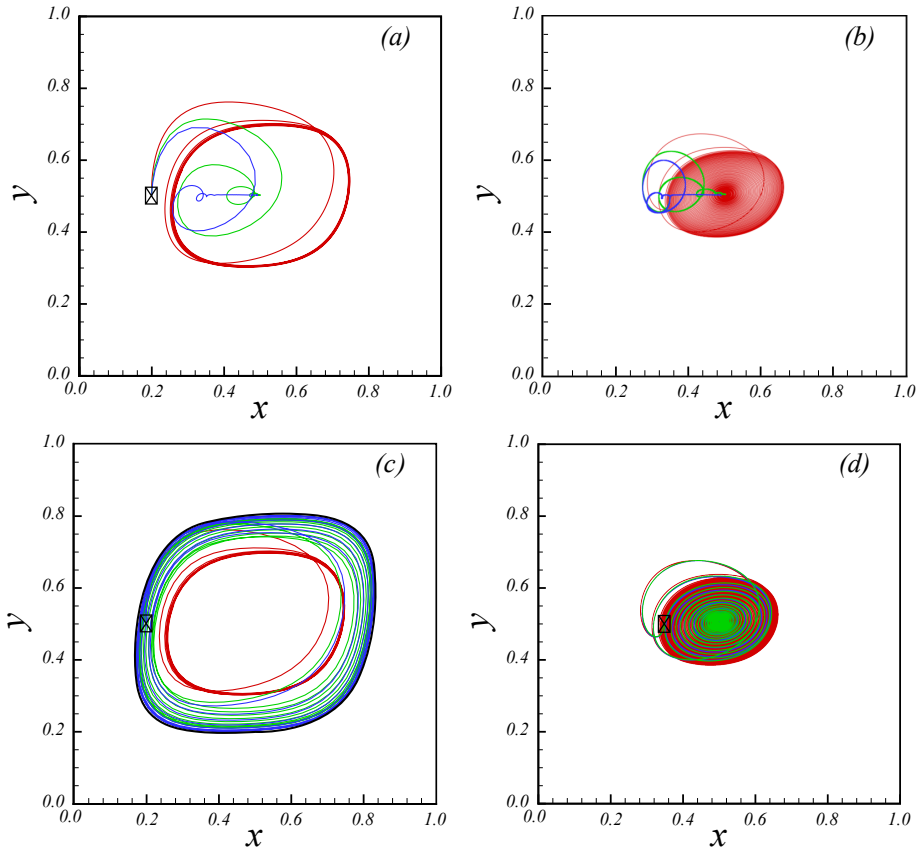

Figure 4.30 – Motion patterns defined by different heat capacity, (a) and (b), and thermal conductivity, (c) and (d), ratios varying between 1 (red lines), 10 (green lines) and 50 (blue lines). Set at $Ra = 10^4$ and $Pr^{amb} = 7.0$, (a) and (c) represent $x_0 = 0.20$, and (c) and (d) represent $x_0 = 0.35$.

Figure 4.30 shows that for λ_C variations, the droplet presented similar behaviors for both releasing positions. Results indicated that for both $Pr^{amb} = 0.70$ and $Pr^{amb} = 7.0$, enhanced values of Pr^{drop} result in this particular rotating motion, defined by short decreasing amplitudes. The droplet moves pass the central region until being dragged towards the enclosure's center. As Pr^{drop} can be also defined as ν^{drop}/α^{drop} and both fluids are assumed to have the same viscosity, results lead to the conclusion that the droplet's thermal diffusion coefficient decrease is behind such behavior.

Increasing values of λ_κ resulted in two different stationary motions, according to the droplet's initial position. When released from $x_0 = 0.20$, the droplet travels towards a

single closed marginal path that diverges from the one observed for $\lambda_\kappa = 1$. The path is described by larger amplitudes and an enhanced inclination. For $x_0 = 0.35$, however, the droplet travels in helical paths towards the center, highlighting that in cases which $\lambda_\kappa > 1$, the releasing position affects the final path.

In conclusion, results indicate that, at $Ra = 10^4$, larger values of λ_κ and λ_C impact directly the droplet motion and path patterns. Consequentially, the droplet's fluid Prandtl number affects significantly the flow's dynamics.

4.7 Nusselt number and heat transfer variations

The Nusselt number represents the non-dimensional temperature gradient at the wall, strictly related to the convective heat transfer coefficient. The effects of the droplet on the system's heat transfer coefficients were evaluated by examining Nu variations when setting $Ra = 1 \times 10^4$, for both $Pr^{amb} = 0.70$ and $Pr^{amb} = 7.0$.

Figure 4.31 shows Nu variation in time for $Pr = 0.70$, considering $x_0 = 0.25$ and $x_0 = 0.35$. Within these initial conditions, the releasing positions did not seem to play a significant role when higher values of λ_C and λ_κ were applied. For increasing values of λ_C, as the motion reaches the center, the Nusselt number is stabilized at the average value Nu_{avg}. For higher conductivity ratios, Nu varies in constant periodical cycles during stationary regime.

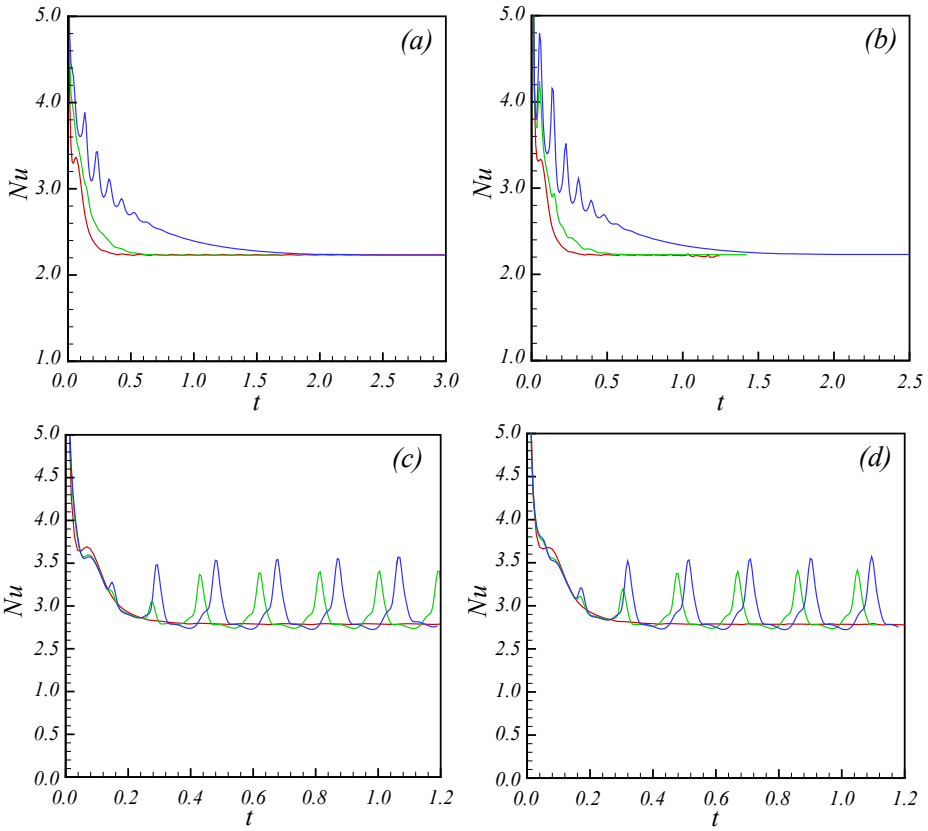

Figure 4.31 – Nusselt number (Nu) variation patterns over time (t), considering $Ra = 10^4$ and $Pr^{amb} = 0.70$. Plots (a) and (b) show results for $\lambda_C = 1$ (red lines), 10 (green lines) and 50 (blue lines), when $x_0 = 0.25$ and 0.35, respectively. Plots (c) and (d) show results for $\lambda_\kappa = 1$ (red lines), 10 (green lines) and 50 (blue lines), when $x_0 = 0.25$ and 0.35, respectively.

The analogous case was analyzed for $Pr^{amb} = 7.0$, considering $x_0 = 0.20$ and $x_0 = 0.35$. Figures 4.32 (a) and (b) show that for both releasing positions, similar Nusselt variation patterns were observed for the three values of λ_C. In contrast, higher thermal conductivity ratios affected the system's heat transfer rate in different manners for each starting point. For $x_0 = 0.20$, as the droplet moves towards the margin, the Nusselt number varies continually until reaching a constant oscillation. This process results in a noticeable Nu_{avg} enhancement, as showed in Fig. 4.32 (c). For $x_0 = 0.35$ the droplet causes similar Nusselt variations for all values of λ_κ. At the begging of the motion, a slight oscillation is observed before the system reaches Nu_{avg}. The average Nusselt number did not suffer any significant changes at the stationary regime.

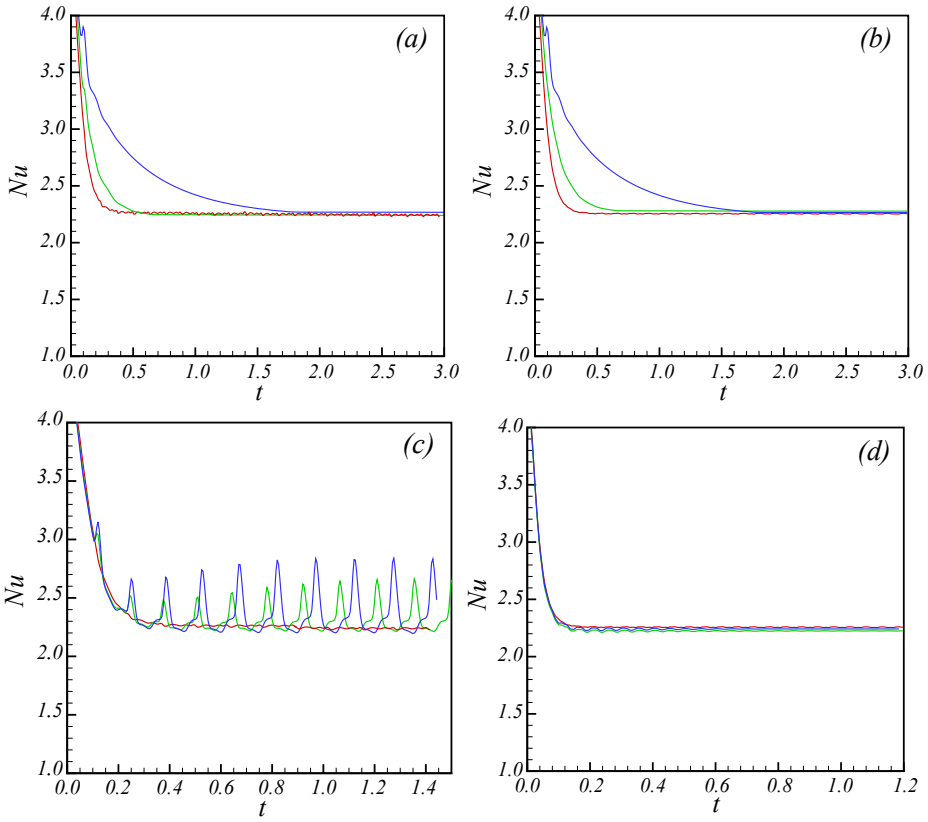

Figure 4.32 – Nusselt number variation patterns considering $x_0 = 0.35$ at (a) and (c) and $x_0 = 0.20$ at (b) and (d) in a flow set at $Ra = 10^4$ and $Pr^{amb} = 7.0$. Plots (a) and (b) show results for $\lambda_C = 1$ (red lines), 10 (green lines) and 50 (blue lines). Plots (c) and (d) show results for $\lambda_\kappa = 1$ (red lines), 10 (green lines) and 50 (blue lines).

A quantitative evaluation of the average Nusselt number was also carried so that the variation ΔNu could be specified. The analogous monophase version of the flow was used as reference, considering that for $Pr^{amb} = 0.70$, $Nu_{avg} = 2.230$ and for $Pr^{amb} = 7.0$, $Nu_{avg} = 2.272$. The values of ΔNu indicate how much the droplet contributed to or jeopardized the system's heat transfer processes.

Initially, the investigations considered effects on Nu_{avg} caused by a moving droplet when $\lambda_C = \lambda_\kappa = 1$. Even though both phases are assumed to have the same thermal properties, and consequentially the same Pr^{drop}, Tab. 6 shows that the presence of the moving droplet provoked small Nu variations. In that sense, the heat transfer coefficient

Table 6 – Nusselt number variations when $\lambda_C = \lambda_\kappa = 1$ is considered for four different cases.

Pr^{amb}	λ_κ	λ_C	x_0	Nu_{avg}	ΔNu
0.70	1	1	0.25	2.244	0.63%
			0.35	2.211	-0.85%
7.00	1	1	0.20	2.262	-0.44%
			0.35	2.254	-0.79%

Tables 7 and 8 display the values of Nu_{avg} and ΔNu calculated for cases in which

$\lambda_C > 1$, and considering $Pr^{amb} = 0.70$ and $Pr^{amb} = 7.0$, respectively. At stationary regime, the droplet remains still at the enclosure's center for all cases in which $\lambda_C \neq 1$. In that sense, for enhanced λ_C, the droplet conserves part of the heat at the enclosure's center. As a result, considerably small Nu variations were observed, indicating that for enhanced λ_C, the droplet has no significant effects on the system's heat transfer processes.

Table 7 – Nusselt number variations observed when setting $\lambda_C > 1$ and $\lambda_\kappa = 1$. The table indicates how different thermal capacity ratios affect ΔNu for each releasing position considered when $Pr^{amb} = 0.70$. No relevant Nu variations were detected.

x_0	λ_C	Nu_{avg}	ΔNu
0.25	10	2.230	0.00%
	50	2.231	0.05%
0.35	10	2.229	-0.04%
	50	2.231	0.05%

Table 8 – Nusselt number variations observed when setting $\lambda_C > 1$, $\lambda_\kappa = 1$ and $Pr^{amb} = 7.0$. the average Nusselt decreases for $\lambda_C > 1$. Since the droplet performs similar paths towards the same final position at the center, same values of λ_C result in same ΔNu.

x_0	λ_C	Nu_{avg}	ΔNu
0.20	10	2.245	-1.19%
	50	2.263	-0.4%
0.35	10	2.245	-1.19%
	50	2.263	-0.4%

When considering $Pr^{amb} = 0.70$ for both releasing positions, the droplet affects the temperature field while moving near the wall region. Results displayed in Tab. 9 indicate a heat transfer enhancement when larger values of λ_κ were considered. Therefore, the system's Nu_{avg} increased, as ΔNu reached values up to 8.12%. As the final path is the same for both releasing positions, within the same value of λ_κ, the average Nusselt number and the respective variation rates are approximately the same.

Table 9 – Nusselt number variations observed when setting $\lambda_\kappa > 1$ and $\lambda_C = 1$. By enhancing the thermal conductivity, Nu_{avg} increases considerably regardless of the releasing position.

x_0	λ_κ	Nu_{avg}	ΔNu
0.25	10	2.363	5.96%
	50	2.411	8.12%
0.35	10	2.372	6.37%
	50	2.403	7.75%

For $Pr^{amb} = 7.0$, as the two analyzed values of x_0 resulted in different stationary paths, it is possible to affirm that the releasing positions affected the system's average Nusselt number. Table 10 shows that for $x_0 = 0.20$, Nu_{avg} enhanced within both values

of λ_κ. For $x_0 = 0.35$, on the other hand, the droplet moves towards the center, resulting in a decrease of Nu_{avg}. In that sense, conclusions lead to the fact that increasing values of λ_κ will only result in relevant heat transfer enhancement when the droplet moves in closed marginal cycles. Furthermore, it has become clear that for $Pr^{amb} = 0.70$, ΔNu reached higher values. Since x_w increases for $Pr^{amb} = 7.0$ as the droplet moves closer to the enclosure's center, one can also conclude that the stationary path's distance from the walls has a direct influence on the flow's heat transfer rates.

Table 10 – Nusselt number variations observed when setting $\lambda_\kappa > 1$, $\lambda_C = 1$ and $Pr^{amb} = 7.0$. Results indicated that when the droplet moves in closed paths near the walls, $\Delta Nu > 0$, and when it settles at the center, $\Delta Nu < 0$.

x_0	λ_κ	Nu_{avg}	ΔNu
0.20	10	2.328	2.46%
	50	2.372	4.40%
0.35	10	2.224	-2.11%
	50	2.241	-1.36%

5 Final Remarks

5.1 Conclusion

The present work displayed an extensive investigation of droplet dynamics in confined natural convection flows. Several aspects were analyzed, enabling the definition of distinct behavior patterns. The work highlighted how the flow's properties can affect both droplet motion and heat transfer coefficients. Furthermore, the study provided important and innovative insights on droplet motion in non-isotherm flows.

As in the monophase case, the Rayleigh number exerts significant influence on the flow's behavior, defining the droplet's motion regime. Several different releasing positions were investigated considering both x_0 and y_0. For lower values of Ra, the paths are described by linear motion in which the releasing positions display no significant influence on the stationary trajectory. For high enough Rayleigh numbers, on the other hand, non-linear motions were detected, revealing that depending on its starting point, the drop can either move in helical motions towards the center or define a closed marginal path. Also, in cases where the droplet moves within the closed path, results indicated that for Ra up to 10^4, a scaling law can be applied to describe the relationship between the droplet's turnover frequency and the Rayleigh number.

The Prandtl number was only noticed to influence the flow's behavior within a defined range. While motion regimes were not affected, the relations between x_w and x_0 have slightly changed. Also, the path's amplitude decreased linearly with Pr enhancement, keeping the droplet closer to the central region and increasing x_w. For high enough Rayleigh numbers, x_w becomes a constant, as Prandtl no longer affects the motion.

Investigating the mechanism behind the behaviors described, it is possible to state that convective currents formed in the flow as a result of Rayleigh enhancement have a considerable influence on the system's non-linearity. The appearance of these currents is responsible for causing noticeable asymmetries in the flow, which affect directly the binary interaction between the velocity field and the interface. Also, the encounter between the core circulation and the droplet at the beginning of the motion defines the helical motion that reaches the enclosure's center.

By varying the values of λ_κ and λ_C, new motion patterns can be detected. For

$Pr = 0.70$, increasing the droplet's thermal conductivity and heat capacity results in the interface migration towards the boundaries and the enclosure's center, respectively. In this particular case, no influence of the releasing position on the final path was observed. When $Pr = 7.0$, increasing values of λ_C drive the droplet to the center, regardless of its starting point. When higher values of λ_κ are considered, the droplet behaves accordingly to Fig. 4.20, moving either towards the center or the margin for the specified releasing positions. As explained in the discussion, both thermal properties' ratios affect the droplet's Prandtl number. In that sense, when $\lambda_C > 1$, $Pr^{drop} > Pr^{amb}$, while for $\lambda_\kappa > 1$, $Pr^{drop} < Pr^{amb}$.

In conclusion, the Nusselt number has been analyzed for several cases, representing the influence of the moving droplet in the system's heat transfer coefficients. Within both Prandtl numbers considered, the system has only accused Nu enhancement when, at stationary regime, droplets with increased κ move in closed cycles near the enclosure. The average Nusselt reached values up to 8.12% larger for $Pr = 0.70$ and 4.40% for $Pr = 7.0$, when $\lambda_\kappa = 50$ was considered. These results represent a significant heat transfer enhancement.

5.2 Future Works

In future works, several aspects that were not emphasized within the present work will be further explored. Among the topics that will be approached next, are

- The effects of droplet's viscosity and density on the flow's dynamics and heat transfer coefficients;
- High deformation regimes, in which Capillary number is enhanced to enable more expressive deformations, and even droplet breakup;
- Resealing multiple smaller droplets at the system. As the dynamics of a single droplet has become more clear after the presented insights, the motion patterns of several moving interfaces should be the next step;
- Heat transfer enhancement and droplet interaction in a confined natural convection flow where an emulsion moves driven by buoyancy.

Bibliography

Ascoli, E. P.; Lagnado, R. R. The linear stability of a spherical drop migrating in a vertical temperature gradient. *Physics of Fluids A: Fluid Dynamics*, v. 4, p. 225–233, 1992. Quoted on page 7.

Assimacopoulos, D. et al. Natural convection flow in a square cavity. *International Journal for Numerical Methods in Fluids*, v. 18, p. 695–719, 1994. Quoted 4 times on pages x, 2, 26, and 27.

Aursand, E. et al. A multi-phase ferrofluidflow model with equation of state forthermomagnetic pumping and heat transfer. *Journal of Magnetism and Magnetic Materials*, v. 402, p. 8–19, 2016. Quoted on page 1.

Barthès-BieseL, D.; Acrivos, A. Deformation and burst of a liquid droplet freely suspended in a linear shear field. *Journal of Fluid Mechanics*, v. 61, p. 1–21, 1973. Quoted 2 times on pages 5 and 6.

Bentley, B. J.; Leal, L. G. An experimental investigation of drop deformation and breakup in steady two-dimensional linear flows. *Journal of Fluid Mechanics*, v. 167, p. 241–283, 1986. Quoted on page 6.

Brown, D. L. et al. Accurate projection methods for the incompressible navier–stokes equations. *Journal of Computational Physics*, v. 168, p. 464–499, 2001. Quoted on page 16.

Cates, M. I.; Tjhung, E. Theories of binary fluid mixtures: from phase-separation kinetics to active emulsions. *Journal of Fluid Mechanics*, v. 836, p. P1–1–68, 2017. Quoted on page 1.

Chen, Y. et al. Dynamic behavior of a deformable bubble rising near a vertical wire-mesh in the quiescent water. *Experimental Thermal and Fluid Science*, v. 120, 2020. Quoted on page 7.

Cunha, L. et al. Field-induced control of ferrofluid emulsion rheology and droplet break-up in shear flows. *Physics of Fluids*, AIP Publishing LLC, v. 30, n. 12, p. 122110, 2018. Quoted on page 2.

Cunha, L. H. P. et al. Effects of external magnetic fields on the rheology and magnetization of dilute emulsions of ferrofluid droplets in shear flows. *Physics of Fluids*, v. 32, p. 073306, 2020. Quoted on page 28.

Dai, Q. W. et al. Contact angle hysteresis effect on the thermocapillary migration of liquid droplets. *Journal of Colloid and Interface Science*, v. 515, p. 32–38, 2018. Quoted on page 1.

Davis, G. D. V. Natural convection of air in a square cavity: A bench mark numerical solution. *International Journal for Numerical Methods in Fluids*, v. 3, p. 249–264, 1983. Quoted on page 26.

Fan, Z. et al. Methyl-grafted silica nanoparticle stabilized water-in-oil pickering emulsions with low-temperature stability. *Journal of Colloid and Interface Science*, Elsevier, v. 588, p. 501–509, 2021. Quoted on page 6.

Fusegi, T. et al. A numerical study of three-dimensional natural convection in a differentially heated cubical enclosure. *International Journal of Heat and Mass Transfer*, v. 34(6), p. 1543–1557, 1991. Quoted on page 26.

Gasanov, B. M. Boiling of disperse-phase droplets in a forced flow of emulsion in a minichannel. *International Journal of Heat and Mass Transfer*, v. 142, 2019. Quoted on page 7.

Gu, J. et al. Influence of rayleigh number and solid volume fraction in particle dispersed natural convection. *International Journal of Heat and Mass Transfer*, v. 120, p. 250–258, 2018. Quoted on page 2.

Guo, Q. et al. Rheological properties and stabilizing effects of high-temperature extracted flaxseed gum on oil/water emulsion systems. *Food Hydrocolloids*, Elsevier, v. 112, p. 106289, 2021. Quoted on page 6.

Hakimi, F.; Schowalter, W. The effects of shear and vorticity on deformation of a drop. *Journal of Fluid Mechanics*, Cambridge University Press, v. 98, n. 3, p. 635–645, 1980. Quoted on page 6.

Huyst, A. M. et al. Detection of ovalbumin amyloid-like fibrils at the oil-water interface in oil-in-water emulsions by spinning disk confocal microscopy. *Food Structure*, Elsevier, p. 100207, 2021. Quoted on page 6.

Ioannou, N. et al. Droplet dynamics in confinement. *Journal of Computational Science*, v. 17(2), p. 463–474, 2016. Quoted 2 times on pages x and 29.

Kefayati, G. H. R. Heat transfer and entropy generation of natural convection on non-newtonian nanofluids in a porous cavity. *Powder Technology*, v. 299, p. 127–149, 2016. Quoted on page 2.

Kempin, M. V. et al. Modeling of water-in-oil pickering emulsion nanofiltration-influence of temperature. *Journal of Membrane Science*, Elsevier, p. 119547, 2021. Quoted on page 6.

Kennedy, M. et al. Motion and deformation of liquid drops, and the rheology of dilute emulsions in shear flow. *Computers & Fluids*, v. 365, p. 205–234, 1994. Quoted 2 times on pages x and 29.

Khalid, M. et al. Effect of nano-clay cloisite 20a on water-in-oil stable emulsion flow at different temperatures. *Journal of Petroleum Science and Engineering*, Elsevier, v. 184, p. 106595, 2020. Quoted on page 6.

Khan, A. et al. Dynamic study of ferrodroplet and bubbles merging in ferrofluid by a simplified multiphase lattice boltzmann method. *Journal of Magnetism and Magnetic Materials*, v. 425, p. 165869, 2018. Quoted on page 1.

Kim, J.; Moin, P. Application of a fractional-step method to incompressible navier–stokes equations. *Journal of Computational Physics*, v. 59, p. 308–323, 1985. Quoted on page 16.

Kwak, S.; Pozrikidis, C. Adaptive triangulation of evolving, closed, or open surfaces by the advancing-front method. *Journal of Computational Physics*, v. 145(1), p. 61–88, 1998. Quoted 2 times on pages x and 29.

Li, J. et al. Numerical simulation of breakup of a viscous drop in simple shear flow through a volume-of-fluid method. *Physics of Fluids*, v. 12, p. 269, 2000. Quoted 2 times on pages x and 29.

Liu, F. et al. Non-fourier heat conduction in oil-in-water emulsions. *International Journal of Heat and Mass Transfer*, Elsevier, v. 135, p. 323–330, 2019. Quoted 2 times on pages 1 and 6.

Liu, N. et al. Stability and in vitro digestion of high purity diacylglycerol oil-in-water emulsions. *LWT*, Elsevier, v. 148, p. 111744, 2021. Quoted on page 6.

Loewenberg, M.; Hinch, E. Numerical simulation of a concentrated emulsion in shear flow. *Journal of Fluid Mechanics*, Cambridge University Press, v. 321, p. 395–419, 1996. Quoted on page 6.

Ma, Y. et al. Numerical study of mhd nanofluid natural convection in a baffled u-shaped enclosure. *International Journal of Heat and Mass Transfer*, v. 130, p. 123–134, 2019. Quoted on page 2.

Markatos, N. C.; Pericleous, K. A. Laminar and turbulent natural convection in an enclosed cavity. *International Journal of Heat and Mass Transfer*, v. 27, p. 772–775, 1984. Quoted on page 26.

Mehryan, S. A. N. et al. Natural convection of magnetic hybrid nanofluid inside a double-porous medium using two-equation energy model. *Journal of Molecular Liquids*, v. 277, p. 959–970, 2019. Quoted on page 2.

Meng, X. et al. Numerical investigation of nanofluid natural convection coupling with nanoparticles sedimentation. *Applied Thermal Engineering*, v. 95, p. 411–420, 2016. Quoted on page 2.

Mohebbi, R.; Rashidi, M. M. Numerical simulation of natural convection heat transfer of a nanofluid in an l-shaped enclosure with a heating obstacle. *Journal of the Taiwan Institute of Chemical Engineers*, v. 72, p. 70–84, 2017. Quoted on page 2.

Nayfeh, A. H. Nonlinear stability of a liquid jet. *The physics of fluids*, American Institute of Physics, v. 13, n. 4, p. 841–847, 1970. Quoted on page 6.

Osher, S.; Fedkiw, R. *Level set methods and dynamic implicit surfaces*. [S.l.]: Springer Science & Business Media, 2006. v. 153. Quoted 2 times on pages 17 and 19.

Ostrach, S. Natural convection in enclosures. *Journal of Heat Transfer*, v. 110, p. 1175–1190, 1988. Quoted on page 2.

Pandey, S. et al. An exhaustive review of studies on natural convection in enclosures with and without internal bodies of various shapes. *International Journal of Heat and Mass Transfer*, v. 138, p. 762–795, 2019. Quoted on page 2.

Qiao, L. et al. Modeling thermocapillary migration of interfacial droplets by a hybrid lattice boltzmann finite difference scheme. *Applied Thermal Engineering*, Elsevier, v. 131, p. 910–919, 2018. Quoted 2 times on pages 1 and 7.

Rallison, J. The deformation of small viscous drops and bubbles in shear flows. *Annual review of fluid mechanics*, Annual Reviews 4139 El Camino Way, PO Box 10139, Palo Alto, CA 94303-0139, USA, v. 16, n. 1, p. 45–66, 1984. Quoted on page 6.

Rallison, J.; Acrivos, A. A numerical study of the deformation and burst of a viscous drop in an extensional flow. *Journal of Fluid Mechanics*, Cambridge University Press, v. 89, n. 1, p. 191–200, 1978. Quoted on page 6.

Shadakofsky, B.; Kulacki, F. A. Boiling of dilute emulsions. mechanisms and applications. *International Journal of Heat and Mass Transfer*, Elsevier, v. 141, p. 1252–1271, 2019. Quoted on page 1.

Siavashi, M. et al. Nanofluid and porous fins effect on natural convection and entropy generation of flow inside a cavity. *Advanced Powder Technology*, v. 29, p. 142–156, 2018. Quoted on page 2.

Sibillo, V. et al. Drop deformation in microconfined shear flow. *Physical Review Letters*, v. 97, p. 054502, 2006. Quoted 2 times on pages x and 29.

Stone, H. A. Dynamics of drop deformation and breakup in viscous fluids. *Annual Review of Fluid Mechanics*, Annual Reviews 4139 El Camino Way, PO Box 10139, Palo Alto, CA 94303-0139, USA, v. 26, n. 1, p. 65–102, 1994. Quoted on page 6.

Sussman, M. et al. An improved level set method for incompressible two-phase flows. *Computers & Fluids*, v. 27, p. 663–680, 1998. Quoted 2 times on pages 12 and 13.

Taylor, G. Conical free surfaces and fluid interfaces. In: *Applied Mechanics*. [S.l.]: Springer, 1966. p. 790–796. Quoted on page 6.

Taylor, G. I. The viscosity of a fluid containing small drops of another fluid. *Proceedings of the Royal Society of London. Series A, Containing Papers of a Mathematical and Physical Character*, The Royal Society London, v. 138, n. 834, p. 41–48, 1932. Quoted on page 6.

Torza, S. et al. Particle motions in sheared suspensions xxvii. transient and steady deformation and burst of liquid drops. *Journal of colloid and interface science*, Elsevier, v. 38, n. 2, p. 395–411, 1972. Quoted on page 6.

Vananroye, A. et al. Effect of confinement on the steady-state behavior of single droplets during shear flow. *Journal of Rheology*, v. 51, p. 139–153, 2007. Quoted 2 times on pages x and 29.

Wang, F.-F. et al. Novel fabrication for 2d mofs-based oil-in-water lubricating emulsion via the self-assembly interface. *Materials Letters*, Elsevier, v. 297, p. 129981, 2021. Quoted on page 6.

Wenzel, E. A. et al. Modeling and simulation of liquid–liquid droplet heating in a laminar boundary layer. *International Journal of Heat and Mass Transfer*, v. 97, p. 653–661, 2016. Quoted on page 7.

Wu, Z.-B. Terminal states of thermocapillary migration of a planar droplet at moderate and large marangoni numbers. *International Journal of Heat and Mass Transfer*, v. 105, p. 704–711, 2017. Quoted on page 1.

Xu, A. et al. Accelerated lattice boltzmann simulation using gpu and openacc with data management. *International Journal of Heat and Mass Transfer*, v. 109, p. 577–588, 2017. Quoted on page 2.

Yap, Y. F. et al. Investigation of two-phase liquid-droplet flow with particle deposition in the heat exchanger. *Journal of Thermal Science and Engineering Applications*, v. 11, p. 1–11, 2019. Quoted on page 7.

Young, N. O. et al. The motion of bubbles in a vertical temperature gradient. *Journal of Fluids Mechanics*, v. 6, p. 350–356, 1959. Quoted on page 7.

Zhang, Y. et al. Experimental evaluation on natural convection heat transfer of microencapsulated phase change materials slurry in a rectangular heat storage tank. *Energy Conversion and Management*, v. 59, p. 33–39, 2012. Quoted on page 1.

Zhou, J. et al. Fast demulsification of oil-water emulsions at room temperature by functionalized magnetic nanoparticles. *Separation and Purification Technology*, Elsevier, v. 274, p. 118967, 2021. Quoted on page 6.